Chapter 4

Synthesis, Band-gap tuning and Conduction mechanism study of (Co, Bi) doped $PbTiO_3$ for Photo-ferroelectric Applications

4.1 Introduction

As discussed in chapter I, a fundamental problem with perovskite oxides is their wide band gap which causes poor absorption of solar light. Perovskite $PbTiO_3$ is the most studied ferroelectric compound with a high curie temperature, thus being a good candidate for ferroelectric devices. Previously, it is reported that, with controlled amount of transition element doping, $PbTiO_3$ can exhibit semiconducting behaviour at room temperature. Various types of the donor or acceptor dopants can be used for lowering the optical band gap of $PbTiO_3$, either by Pb-site doping or Ti-site doping in the $PbTiO_3$ lattice. To reduce the band gap of $PbTiO_3$, various elements such as Mg, Al, Cr, Fe, Co, Zn, Ga, In, Ni etc, has been used to substitute the Ti- in the $PbTiO_3$ lattice [W. Zhou et al. (2016)]. Though, for most of these dopants the optical band gap of $PbTiO_3$ is reduced but not low enough to use in solar cells.

A suitable ferroelectric semiconductor for photovoltaic application should have both a large ferroelectric polarization and low optical band gap. Low band gap of material helps to absorb more photons and electric field due large polarization improves the ability to separate the photocarriers for current generation. Since Cobalt is a magnetic ion, Co doped $PbTiO_3$ system may offer an interesting combination of ferroelectric and magnetic characteristics for multiferroic device applications. When $PbTiO_3$ is doped with Co, the band gap of material is shifted toward visible region of light [E. Mete et al. (2019)]. F. Azough et al reported that Co doping in $BiFeO_3$ ceramics enhanced the densification process and ferromagnetism [F. Azough et al. (2010)]. It is reported that Co doping in $BiFeO_3$ nanocrystals also reduces the leakage current density [A. K. Sinha et al. (2020)]. M. H. Garrett et al have reported that Co-

doped $BaTiO_3$ ceramics have shown light-induced absorption due to creation of traps [M. H. Garrett et al. (1992)]. The addition of Co creates an absorption peak in visible region which increases with additional Co doping and extends from band edge to visible region [M. H. Garrett et al. (1992)]. Cobalt is associated with an oxygen vacancy complex (Co^{3+}-V_o) that is related to a deep level 2.0-2.3 eV above the valence band in Co-doped $BaTiO_3$ [Rytz et al. (1990)]. It is reported that Co doping help to reduce the band gap of ABO_3 structured materials but it also diminishes the ferroelectric property due to occurrence of oxygen vacancies. In $BaTiO_3$, Co-doping increased the saturation magnetization but decrease in remnant polarization is also reported [A. Rani et al. (2018)].

This chapter presents the results of study of the optical band gap of $xPbTiO_3$-(1-x)$Bi(Co_{1/2}Ti_{1/2})O_3$ solid solution in the composition range ($0.55 \leq x \leq 0.80$). In order to get low band gap material with suitable ferroelectricity, we used Bi^{3+} and Co^{2+} doping to design a new perovskite ferroelectric solid solution $xPbTiO_3$-(1-x)$Bi(Co_{1/2}Ti_{1/2})O_3$. Here, Co^{2+} acts as band gap reducing element while Bi^{3+} will maintain the ferroelectric nature due to its $6s^2$ lone pair electron configuration [P. Baettig et al. (2005)]. A new perovskite ferroelectric solid solution $xPbTiO_3$-(1-x)$Bi(Co_{1/2}Ti_{1/2})O_3$ [xPT-(1-x)BCT] was synthesized by solid state reaction method and its physical properties were investigated with varying the Co doping. In this study, we mainly demonstrate the effect of Co/Ti stoichiometric ratio change on optical band gap of xPT-(1-x)BCT. To confirm the photovoltaic nature of xPT-(1-x)BCT ceramics, photovoltaic cells with device structure Ag/PT-BCT/FTO (Fluorine-doped tin oxide) are fabricated and their electrical properties are discussed.

4.2 Experimental

Various compositions of $xPbTiO_3$-$(1-x)Bi(Co_{1/2}Ti_{1/2})O_3$ (x= 0.80, 0.70, 0.65, 0.60 and 0.55) and $0.60PbTiO_3$-$0.40Bi(Co_yTi_{1-y})O_3$ (y= 0.45, 0.50, 0.55, and 0.60) solid solution powders were synthesized by conventional solid state ceramic method. The details of synthesis route are presented in chapter-2. Stoichiometric weights of constituent oxides, i.e., Bi_2O_3, TiO_2, Co_2O_3 and PbO were first mixed with the help of mortar-pestle. The mixed powders were ball-milled in acetone medium with zirconia ball. The ball milled powders were calcined in the temperature range 600 ^oC to 950 ^oC inside furnace. Powder X-ray diffraction (XRD) measurements were performed at room temperature from 20^o to 120^o using RIGAKU MINIFLEX 600 powder diffractometer with Cu-K_α radiation. Crystal structure analysis was done by Rietveld refinement using FULLPROF suite [J. R. Carvajal (1993)]. The microstructures of as prepared PT-BCT ceramics were examined using scanning electron microscope (ZEISS, Evo 18 Research). The ferroelectric polarization as a function of external field was examined by ferroelectric loop tester based on standard Sawyer-Tower circuit (Radiant Technologies) in frequency range from 1 to 1000 Hz at room temperature. The Ultra-Violet-visible absorbance spectra was recorded at room temperature using Spectrophotometer (Horiba Jobin Yvon) and the optical band gap was calculated by Tauc equation. In order to study ferroelectric photovoltaic phenomenon in PT-BCT, thin films of 0.60PT-0.40BCT composition were deposited on FTO coated glass substrates by magnetron sputtering. The surface morphology and ferroelectric switching behavior of 0.60PT-0.40BCT films at nanoscale was visualized by using PFM. The current-voltage (I-V) measurement of as prepared device was measured using Keithley 2400 source-meter interfaced with a computer. The local I-V curve of

PT-BCT films were recorded using C-AFM under light and dark. A green laser light (wavelength ~ 532 nm, 5 mW to 50mW power) was used to illuminate the surface.

4.3 Results and Discussion

4.3.1 Effect of Calcination Temperature on $xPbTiO_3$-(1-x)$Bi(Co_{1/2}Ti_{1/2})O_3$ (x=0.60)

To optimize the calcination temperature and investigate the effect of sample's calcination temperature on structural, morphological properties, we first calcined the reactant powder mixture of 0.60PT-0.40BCT from 600°C to 850°C in air atmosphere for 5 hours duration. The XRD patterns of 0.60PT-0.40BCT powder calcined at various temperatures are shown in Fig.4.1. It is evident from this figure that samples calcined at 800°C and 850°C show good crystallinity and pure perovskite phase. Indexing of the XRD peaks for the sample reveals that the solid solution crystallizes into tetragonal crystal structure with space group *P*4*mm* similar to pure $PbTiO_3$. Samples calcined at 600°C and 700°C reveals few small impurity peaks (marked by *) in addition to the peaks of the perovskite phase. The small peak at 2θ= 27.5° is due to unreacted TiO_2 phase and peak at 2θ= 31.5° is assigned to secondary $PbTi_3O_7$ phase. Thus, the optimum calcination temperature for PT-BCT sample is 800°C for getting pure perovskite phase. It is notable that the splitting of the XRD peak around 2θ= 45° into a doublet, characteristic of the tetragonal structure, is clearly observed for all the samples prepared at various temperatures. Even though the structure is tetragonal for all the samples but the lattice parameters change with calcination temperature. The variation of lattice parameters with calcination temperature for 0.60PT-0.40BCT is shown in Fig.4.2. The tetragonal c parameter increases with increasing the calcination temperature while a- shows small variation. Thus, the tetragonality of the samples is increasing with the calcination temperature of the sample.

Fig. 4.3 shows the scanning electron microscopy (SEM) images of the calcined

samples. As shown in Fig.4.1, the XRD peaks are seen to sharpen with increasing calcination temperature which can be linked with the enhanced grain size. Increased grain size with increasing the calcination temperature is confirmed by SEM images shown in Fig. 4.3. It is observed that 0.60PT-0.40BCT ceramic mostly consists of bigger micron sized grains (1µm- 6 µm) along with few smaller grains having size distribution ranging from 150 nm-300 nm. The average particle size increases from 940 nm to 6.2 µm with increasing the calcinations temperature from 600°C to 950°C. The calcined particles are non-uniform and irregular in shape and size.

Fig. 4.4 (a) and Fig. 4.4(b) show the high resolution-transmission electron microscopy (HR-TEM) images of 0.60PT-0.40BCT sample, calcined at 600°C and 850°C, respectively. Similar to the SEM and XRD results, the HR-TEM images also confirm the increase in particle size with increasing the calcinations temperature. Fig. 4.4 (c) and Fig 4.4 (d) show the selected area electron diffraction (SAED) patterns of 0.60PT-0.40BCT samples, calcined at 600°C and 850°C, respectively. As seen in these figures, the clearly resolved diffraction spots corresponding to crystalline domains are present. The SAED spectra confirm that with increasing the calcination temperature the crystalline nature of materials improved. Fig. 4.5 shows energy dispersive X-ray spectra (EDS) of 0.60PT-0.40BCT (y=0.50) samples calcined at 850°C, along with the elemental maps. The EDS analysis confirms the presence of Bi, Co, Pb, and Ti with no other impurity element. The compositional analysis from EDS reveals that elements are present in the ratio as per the nominal composition of the sample. The elemental maps reveal uniform distribution of elements showing good homogeneity of the sample.

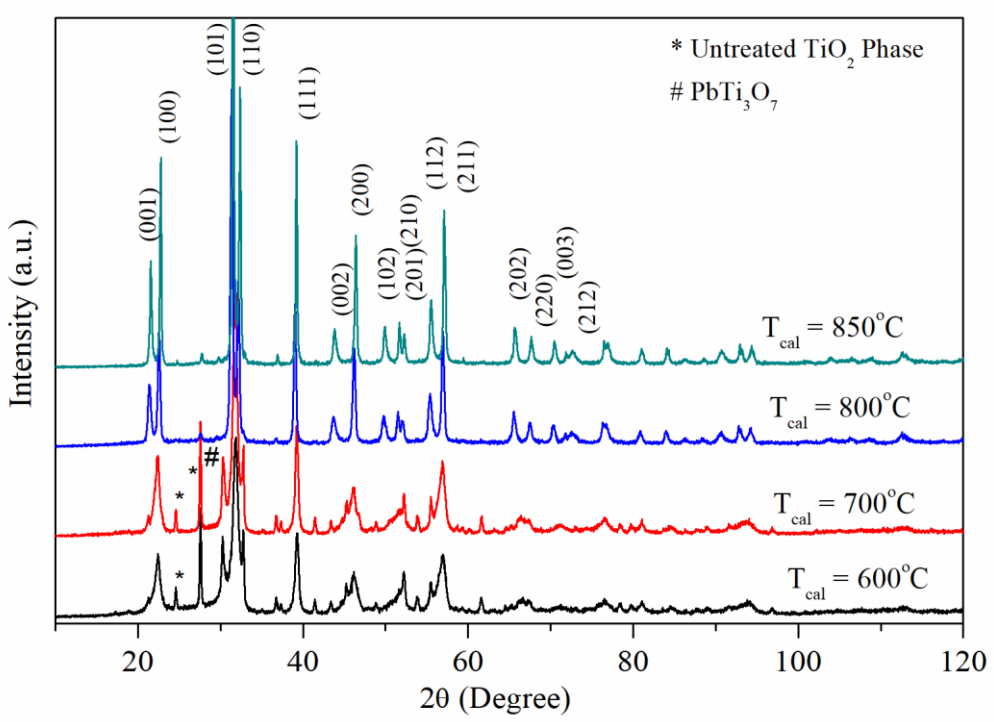

Figure 4.1 Comparison of XRD patterns of $0.60PbTiO_3–0.40Bi(Co_{0.5}Ti_{0.5})O_3$ ceramic powders calcined at various temperatures for 5 hours.

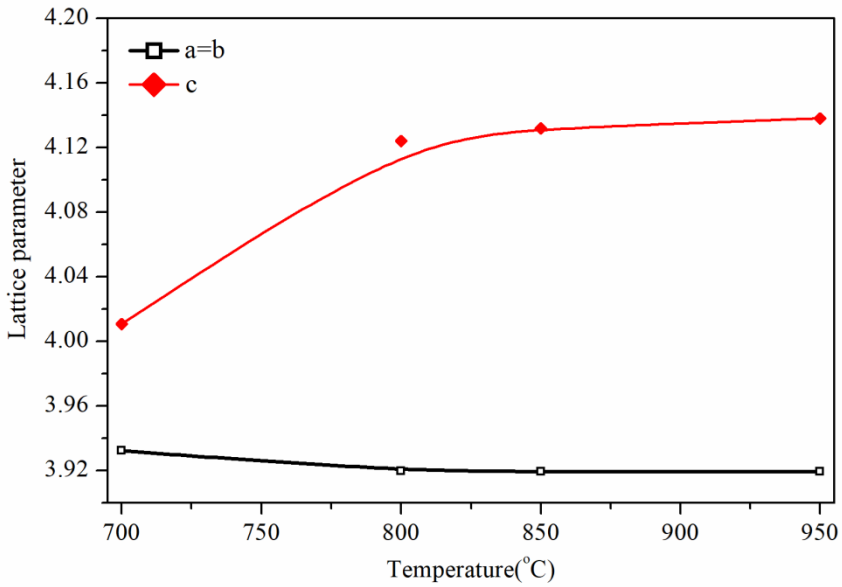

Figure 4.2 Calcination temperature dependent lattice parameters for $0.60PbTiO_3–0.40Bi(Co_{0.5}Ti_{0.5})O_3$ ceramic.

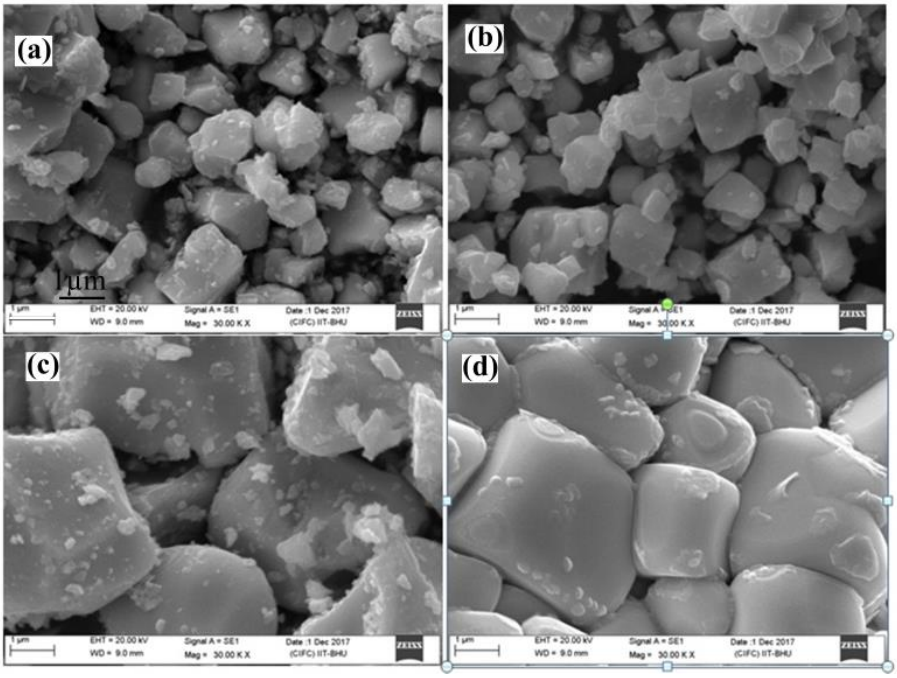

Figure 4.3 SEM images of as synthesized polycrystalline $0.60PbTiO_3$–$0.40Bi(Co_{0.5}Ti_{0.5})O_3$ ceramic calcined for 5 hours at (a) 600°C (b) 700°C (c) 850°C (d) 950°C.

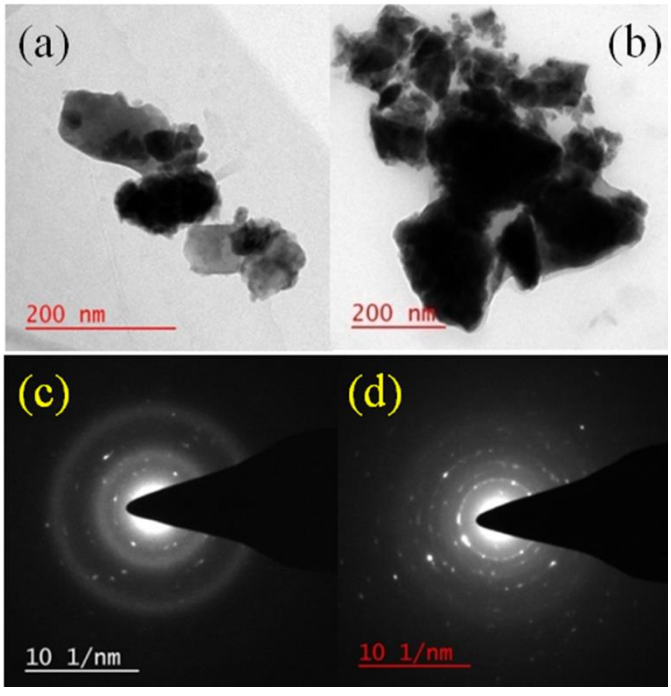

Figure 4.4 HR-TEM images of as synthesized polycrystalline $0.60PbTiO_3$-$0.40Bi(Co_{0.5}Ti_{0.5})O_3$ particles calcined at (a) 600°C (b) 850°C and SAED pattern for particles of samples calcined at (c) 600°C (d) 850°C.

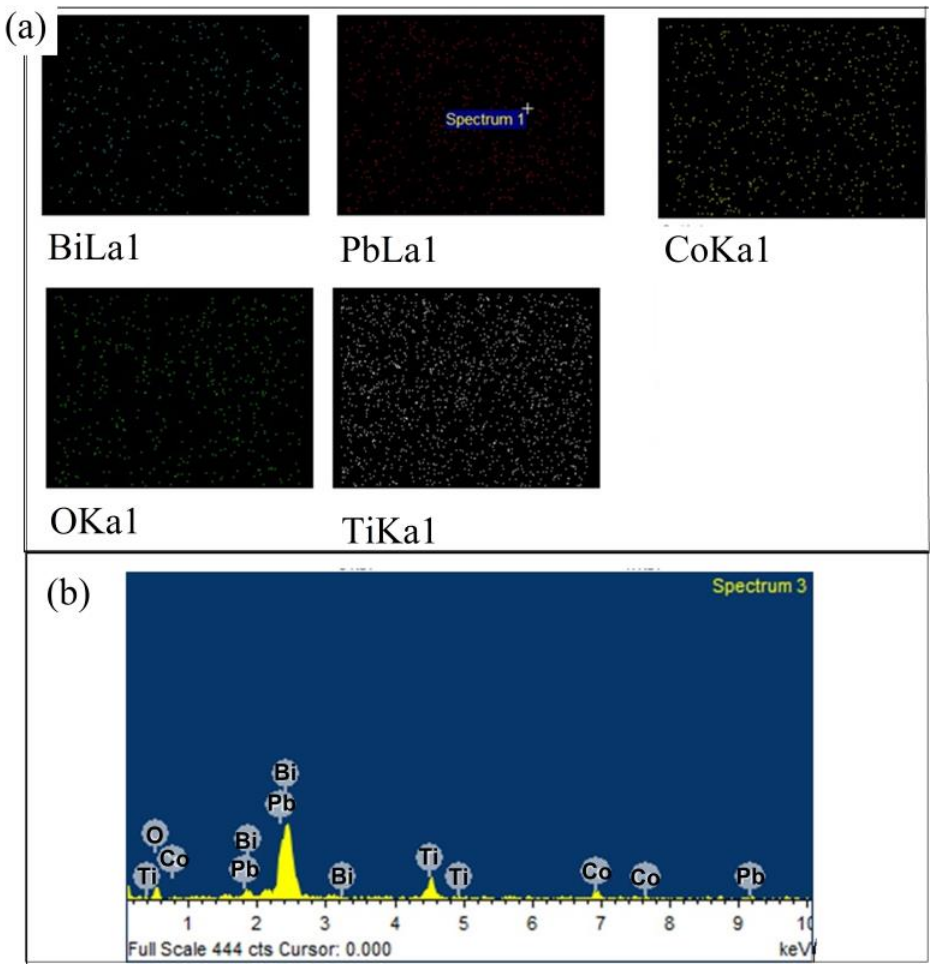

Figure 4.5 Elemental Mapping and EDAX for $0.60PbTiO_3$–$0.40Bi(Co_{0.5}Ti_{0.5})O_3$ particles calcined at 850°C.

4.3.2 Composition Dependent Crystal Structure, Ferroelectric, and Semiconducting Properties of $xPbTiO_3$-$(1-x)Bi(Co_{1/2}Ti_{1/2})O_3$ Solid Solution in the Composition range ($0.55 \leq x \leq 0.80$)

To investigate the composition dependent crystal structure and the physical properties, the PT-BCT samples of various compositions were sintered at optimum temperature of 1000 ^oC for 2 hours. The sintering was done inside the MgO powder sealed Al-crucible with sacrificial Bi_2O_3 and PbO powders to compensate for the volatile Bi-Pb-oxide losses at higher temperatures. Room-temperature XRD patterns for sintered samples of $xPbTiO_3$-$(1-x)Bi(Co_{1/2}Ti_{1/2})O_3$ solid solution in the composition range ($0.55 \leq x \leq 0.80$), are shown in Fig. 4.6. These XRD data show that sintered PT-

BCT ceramic samples also have the perovskite structure. The XRD patterns of compositions rich in BCT have few additional weak reflections corresponding to secondary phase. Presence of small non-perovskite secondary phase on the Bi-rich end compositions is reported in other Bi-based solid solutions of $PbTiO_3$ also [R. Pandey et al. (2014)]. The XRD peaks of all the compositions are well matched corresponding to the tetragonal structure similar to $PbTiO_3$. The large angular separation between (002) and (200) peaks demonstrate the high tetragonality of the structure for PT-BCT compositions. With increase in BCT concentration, the separation between (002) and (200) peaks increase which can be attributed to the substitution of larger Co^{2+} cations (0.72Å) for smaller Ti^{4+} cations (0.68Å). The larger ionic radius of Co^{2+} also causes a small structural lattice expansion, thus Co^{2+} doping can promote the lattice distortion which may be a factor for higher tetragonality.

To confirm further the tetragonal structure for various compositions of PT-BCT, we performed the Rietveld structural analysis of the x-ray diffraction profiles considers the *P*4*mm* space group. In the process of Rietveld refinement, we considered the substitution of Bi^{3+} ions on Pb-site, while Co^{2+} ions on Ti-site. In the tetragonal phase with *P*4*mm* space group, the Pb^{2+}/Bi^{3+} ions occupy 1(a) sites at (0, 0, 0), Ti^{4+}/Co^{2+} ions occupy 1(b) sites at (1/2, 1/2, ½+δz) and O^{2-}(1) occupy 1(c) sites at (1/2, 1/2, 0+δz), and O^{2-}(2) occupy 2(d) sites at (1/2, 0, 1/2+δz). Fig. 4.7 shows the Rietveld fit for the XRD profile of a representative composition 0.60PT-0.40BCT. The red dots in Fig. 4.7 indicate the experimental XRD data while the Rietveld calculated XRD pattern is shown by the continuous curve overlapping the observed experimental data. The lowest curve shows the difference between observed and calculated XRD profiles. The vertical bars between fitted and difference profiles indicate the positions of Bragg's reflections. A very good fit between observed and calculated XRD patterns seen in Fig. 4.7

confirms the tetragonal structure with *P4mm* space group. The Rietveld structural analysis of the XRD patterns for the other compositions also gives very good fit for the tetragonal structure with space group *P4mm*. Table 4.1, 4.2 and 4.3 are presenting the refined lattice parameters and Rietveld refined structural paramters for majority phases in the composition range $0.55 \leq x \leq 0.80$. The tetragonality is slightly increases with BCT doping but further decreased for x = 0.55 composition. It is found that Bi-O bond length decreases from 2.571Å to 2.5253 Å. The Co-O1 bond length also decreases from 1.34 Å to 1.306 Å with $Bi(Co_{1/2}Ti_{1/2})O_3$ contents doping. The bond angle Bi-O2-Bi increases from 99.2º to 101.954º with increasing the $Bi(Co_{1/2}Ti_{1/2})O_3$ contents doping in PT-BCT.

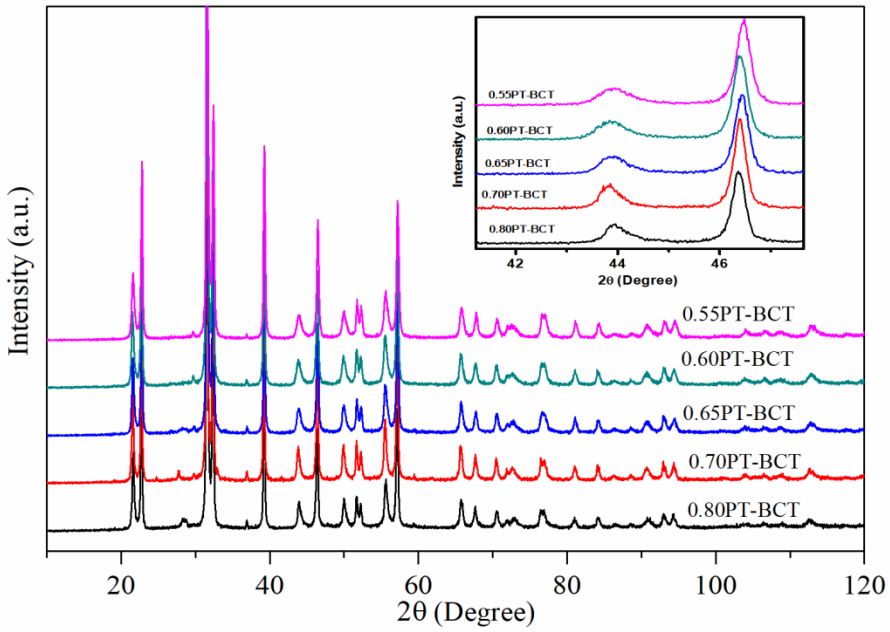

Figure 4.6 Powder x-ray diffraction patterns of $xPbTiO_3$-$(1-x)Bi(Co_{1/2}Ti_{1/2})O_3$ solid solution in the composition range ($0.55 \leq x \leq 0.80$) sintered at 1000 ^oC for 2 hours. The inset shows the zoomed portion for 2θ=43°-49°, to show tetragonal splitting of diffraction peaks with increasing the $Bi(Co_{1/2}Ti_{1/2})O_3$ contents.

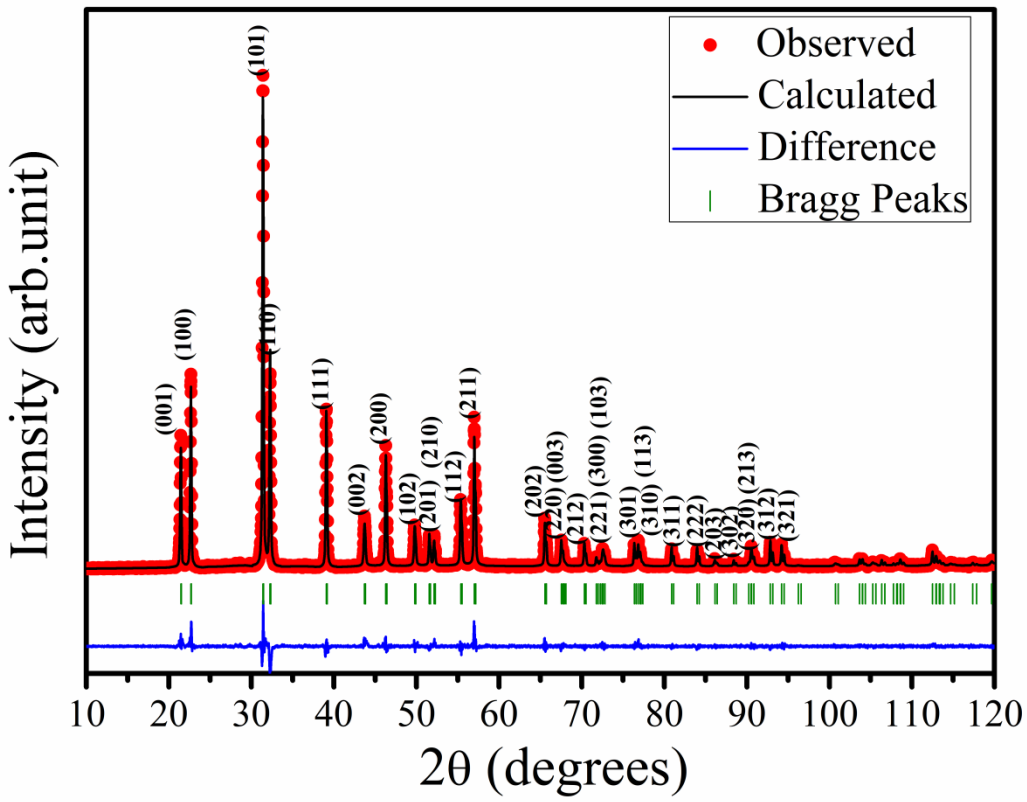

Figure 4.7 Rietveld fit for the XRD pattern of sintered sample of $0.60PbTiO_3$–$0.40Bi(Co_{0.5}Ti_{0.5})O_3$ ceramic. Dots indicate experimental XRD data, while calculated XRD pattern is shown by continuous line. The lower curve shows the difference between experimental and calculated XRD patterns. Vertical bars indicate position of Bragg's peaks.

Table 4.1. Refined Lattice parameters of $(1-x)Bi(Co_{1/2}Ti_{1/2})O_3$-$xPbTiO_3$ for the majority phases in the composition range $0.55 \leq x \leq 0.80$.

`

(1-x)BCT-xPT Compositions (x)	Lattice parameters	
	a=b (Å)	c (Å)
0.55	3.92375 (4)	4.12250 (5)
0.60	3.91925 (2)	4.13792 (1)
0.65	3.91964 (3)	4.12860 (4)
0.70	3.91829 (4)	4.12700 (5)
0.80	3.91657 (2)	4.12469 (2)

Table 4.2. Rietveld refined structural parameters of (1-x)Bi($Co_{1/2}Ti_{1/2}$)O_3-x$PbTiO_3$ for the majority phases in the composition range $0.55 \leq x \leq 0.80$.

X = 0.55 (P4mm)					
Element	**X**	**Y**	**Z**	**B**	**Occupancy**
Pb	0.000	0.000	0.000	2.534 (1)	0.55
Bi	0.000	0.000	0.000	2.570 (1)	0.45
Co	0.500	0.500	0.44886 (2)	0.366 (1)	0.225
Ti	0.500	0.500	0.44886 (2)	0.366 (1)	0.775
O1	0.500	0.500	0.13188 (5)	2.427 (6)	1.000
O2	0.500	0.000	0.61430 (3)	1.329 (3)	2.000
x = 0.80 (for P4mm)					
Pb	0.000	0.000	0.000	1.473 (7)	0.800
Bi	0.000	0.000	0.000	1.509 (7)	0.200
Co	0.500	0.500	0.46342 (3)	0.304 (1)	0.100
Ti	0.500	0.500	0.46342 (3)	0.305 (1)	0.900
O1	0.500	0.500	0.13833 (4)	0.035 (5)	1.000
O2	0.500	0.000	0.59637 (3)	0.326 (3)	2.000

Table 4.3 Rietveld refined structural parameters of (1-x)Bi($Co_{1/2}Ti_{1/2}$)O_3-x$PbTiO_3$ for the majority phases in the composition range $0.55 \leq x \leq 0.80$.

Bond length (Å**) & Angles (**deg.)	**Compositions**				
	x=0.55	**x=0.60**	**x=0.65**	**x=0.70**	**x=0.80**
Pb-Pb/ Bi-Bi	c-4.1225(6), a/b-3.9238(5)	4.13806(1), 3.91910(1)	4.1289(6), 3.9196(5)	4.1270(6), 3.9183(5)	4.1247(3), 3.9166(2)
Pb-O2/ Bi-O2	2.5253(2)	2.518(6)	2.5342(2)	2.559(8)	2.571(9)
Co/Ti-O1	1.30675(1)	2.249(2)	1.16720(1)	1.31(3)	1.34(3)
Co/Ti-O2	2.0771(2)	1.9776(2)	2.0802(2)	2.057(5)	2.034(6)
Bi-O2-Bi	101.954(9)	102.2(3)	102.2(3)	99.9(5)	99.2(5)
O2-Ti-O2	83.8096(1)	88.96(8)	88.96(8)	84.7(3)	85.8(3)

Fig. 4.8 depicts the SEM images of sintered samples of $xPbTiO_3$-(1-x)$Bi(Co_{1/2}Ti_{1/2})O_3$ com positions with x = 0.70 and 0.65. It is observed that grain size and microstructure of PT-BCT ceramics is affected by the BCT content. With increasing BCT content, the grain size reduces. For 0.70PT-BCT, grain size is in the range of 3.5µm- 9.8µm while for 0.65PT-BCT grain size decreases in the range of 2.7 µm – 6.2 µm. For 0.60PT-BCT, the grain size is in the range from 1.0 µm to 3.5 µm. The SEM images reveals that with increasing the BCT content, the grain size reduces but non-uniformity in grain size increases. The EDX map of PT-BCT is shown in Fig. 4.8 (b) and Fig. 4.8 (d) which reveals the presence of Pb, Ti, Co, Bi, and O elements. There is no other impurity element. Table 4.4 provide the experimentally observed and theoretically calculated atomic percentages for the Pb, Ti, Bi, Co, and O atoms present in $0.70PbTiO_3$-$0.30Bi(Co_{1/2}Ti_{1/2})O_3$ obtained from EDS measurements.

Table 4.4: Experimentally observed and theoretically calculated atomic percentages for the Pb, Ti, Bi, Co, and O atoms present in $0.70PbTiO_3$-$0.30Bi(Co_{1/2}Ti_{1/2})O_3$ obtained from EDS measurements.

$0.70PbTiO_3$-$0.30Bi(Co_{1/2}Ti_{1/2})O_3$		
Elements	**Theoretical atomic %**	**Experimental atomic %**
Pb M	14.00	11.93
Ti K	17.00	15
Bi M	6.00	5.29
Co K	3.00	3.39
O K	60.00	64

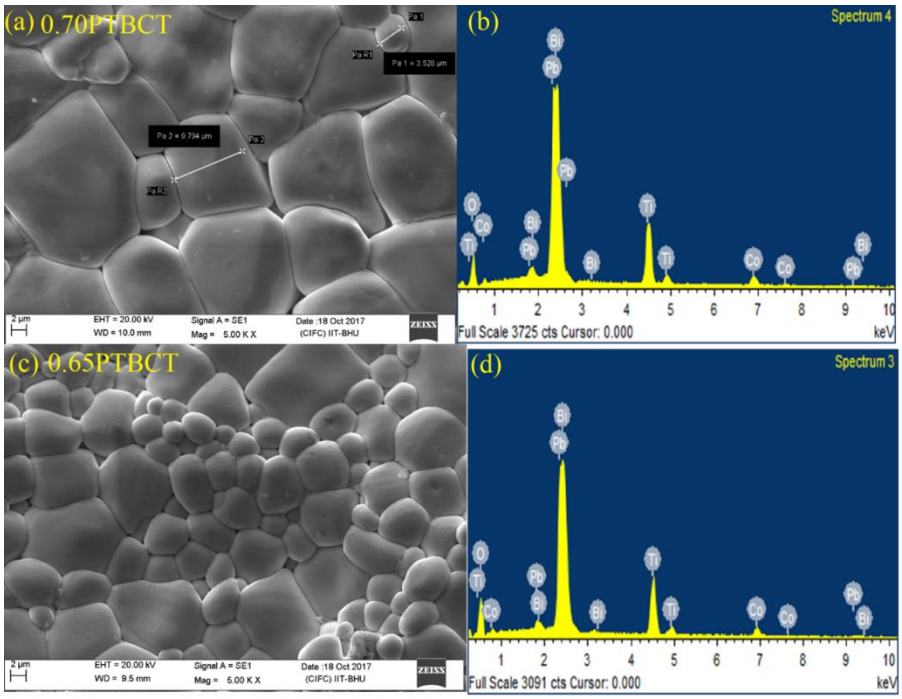

Figure 4.8 The Scanning electron microscopy (SEM) images of (a) 0.70PT-BCT and (c) 0.65PT-BCT ceramics, (b) and (d) showing the corresponding Energy dispersive X-ray spectroscopy (EDS) spectrum.

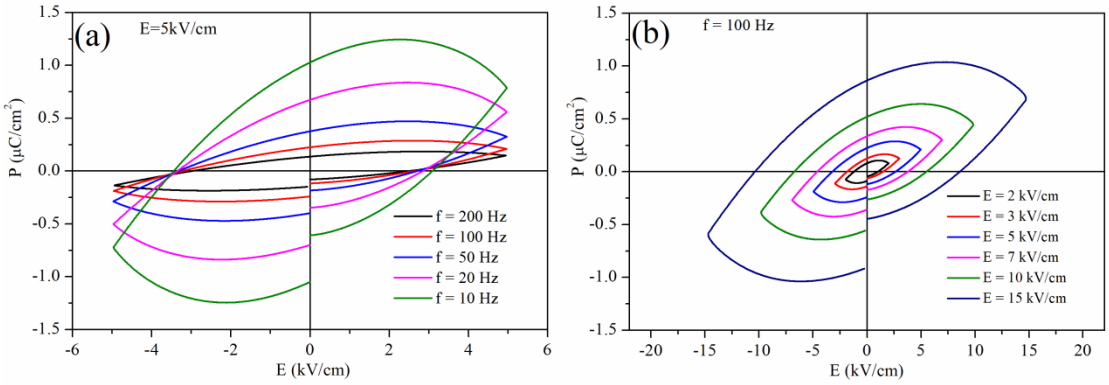

Figure 4.9 Room temperature P-E hysteresis loops of the 0.80PT-0.20BCT as a function of (a) frequency with fixed applied electric field 5kV/cm (b) P-E loops as a function of Electric Field with fixed frequency 100Hz.

Fig. 4.9 (a) shows P-E hysteresis loops of the 0.80PT-0.20BCT capacitor measured at E= 5 kV/cm at various frequencies (f = 10, 20, 50, 100, 200 Hz) which indicates that 0.80PT-BCT ceramics contain good ferroelectricity. Fig. 4.9 (b) depicts the P-E loops of 0.80PT-0.20BCT capacitor measured at f = 100Hz with varying the

electric field (E = 2, 3, 5, 7, 10, and 15 kV/cm). It can be seen that the shape of the P-E hysteresis loop does not depend on applied electric field. The hysteresis loops are little lossy also due to leakage currents contributions. In 0.80PT-0.20BCT capacitor a P_r of 0.86 μC/cm^2 and E_c of 8.47 kV/cm are observed under the electric field of 15 kV/cm as shown in Fig. 4.9. The remnant polarization (P_r) increases with increasing the applied electric field. The low P_r value is due to large leakage currents of the capacitor which makes the 0.80PT-0.20BCT ceramic difficult to be fully polarized, since its coercive field (E_c) always varies with the applied electric field.

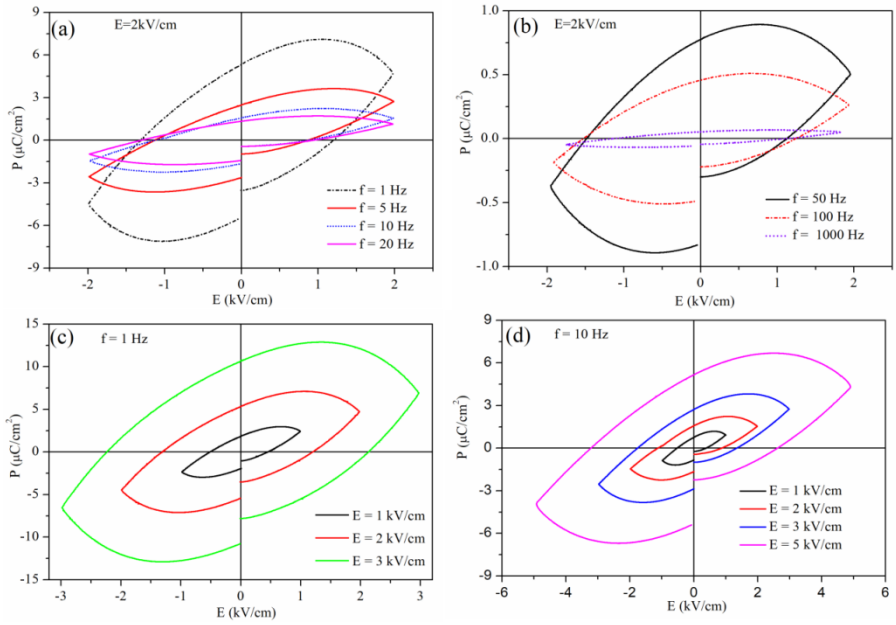

Figure 4.10 Room temperature P-E hysteresis loops of the 0.60PT-0.40BCT (a) and (b) as a function of frequency; P-E loop as a function of Electric Field at a fixed frequency (c) 1 Hz and (d) 10 Hz.

Another Composition 0.60PT-0.40BCT also shows similar ferroelectric nature with slight increase in P_r value as shown in Fig. 4.10. The P-E loop of 0.60PT-0.40BCT shows similar behaviour with changing the applied frequency and electric field. It is observed that with increasing the BCT content the P_r increases while E_c decreases. At fixed frequency (f= 10Hz) and electric field (E = 5kV/cm), the P_r value is 1.04 μC/cm^2

for 0.80PT-0.20BCT while it increases to 5.19 μC/cm^2 for 0.60PT-0.40BCT composition.

4.3.3 Composition Dependent Optical Band Gap Analysis of $xPbTiO_3$-(1-x)$Bi(Co_{1/2}Ti_{1/2})O_3$ Solid Solution in the Composition Range ($0.80 \leq x \leq 0.55$)

The influence of doping percentage on the band gap of $xPbTiO_3$-(1-x)$Bi(Co_{1/2}Ti_{1/2})O_3$ solid solution in the composition range ($0.80 \leq x \leq 0.55$) was characterized by the light-absorption measurements using UV-visible spectroscopy. The optical absorption spectra for various compositions of PT-BCT are shown in Fig. 4.11 (a). The absorption peaks at 410 nm and 607 nm were observed distinctly in 0.80PT-0.20BCT sample. The undoped $PbTiO_3$ shows absorbance peak at 400 nm which shifts toward a larger wavelength with increasing the BCT doping percentage. This shift of absorption edge toward larger wavelength is indication of lowering of optical band gap. The Tauc equation $(\alpha h\upsilon)^{0.5}$ vs $h\upsilon$ plots have been used to calculate the indirect band gap for $xPbTiO_3$-(1-x)$Bi(Co_{1/2}Ti_{1/2})O_3$ solid solution as shown in Fig. 4.11 (b). It is observed that after extrapolating the tangent it provides unrealistic values which indicate that this material does not possess the indirect band gap. The Tauc equation $(\alpha h\upsilon)^2$ vs $h\upsilon$ plots for direct band gap provide reasonable band gap values as inferred from Fig. 4.11 (c). For reference, the Tauc equation $(\alpha h\upsilon)^2$ vs $h\upsilon$ plot for the $PbTiO_3$ is also shown in Fig.4.11(d). In view of the foregoing, the band gaps of all the compositions were determined by extrapolating the linear part of the $(\alpha h\upsilon)^2$ versus $(h\upsilon)$ plots, where $h\upsilon$ is band gap energy and α is absorption coefficient [J. Tauc et al. (1966)] as shown in Fig. 4.12.

The undoped $PbTiO_3$ shows an optical band gap 2.9 eV which reduces to 1.98 eV with 20% BCT (x = 0.80) doping. As shown in Fig. 4.12 (a), two different band gaps E_{g1} = 1.98 eV and E_{g2} = 1.58 eV were featured in $(\alpha h\upsilon)^2$ vs $h\upsilon$ plot for 0.80PT-

0.20BCT composition. Both band gaps reduce to lower values with increasing BCT concentration up to 0.40 as can bees seen from Fig.4.12(b), (c). The band gap values reduce to E_{g1} = 1.83 eV and E_{g2} = 1.37 eV for 0.60PT-0.40BCT. In the 0.55PT-0.45BCT composition depicted in Fig.4.12(d), no further lowering of the band gap is seen. However, all the studied PT-BCT compositions show two direct band gaps. The E_{g1} band gap feature is stronger and visible in Tauc plot as for this region the absorption is high. The direct band gap E_{g1} arises from p-d charge-transfer excitations. The band gap at lower energy side E_{g2} arises from hybridization of Co ($3d_z^2$+O2p_z) and Co-3d excitations [B. S. Holinsworth et al. (2015)]. The E_{g2} feature is weaker in intensity which may be due to lower number of density of states. The decrease in band gap values with increasing the BCT content can be assigned to new states of valence band maximum ($3d_z^2$) and conduction band minimum ($3d_{x^2-y^2}$) in the electronic structure with presence of Co-3d and oxygen vacancies [E. Mete et al. (2019)]. In PT-BCT, band gap value was reduced due to the formation of oxygen vacancies and sub-band gap energy levels, through B-site non-equivalence substitution. Co-ions are introducing sub-bands inside $PbTiO_3$ energy bands. These sub-bands are forming continuous energy band with the conduction band [J. W. Bennett et al. (2008)]. Fig. 4.13 gives schematic representation for the mechanism of band gap lowering due to formation of sub-band between valence and conduction bands. The position of E_{g1} and E_{g2} band gap is explained by showing the sub-band states. The changes in bond length and bond angle values with doping also affect the band gap of PT-BCT. The Co-O1 bond length decreases and Bi-O2-Bi bond angle increases with BCT doping as presented in table 4.3.

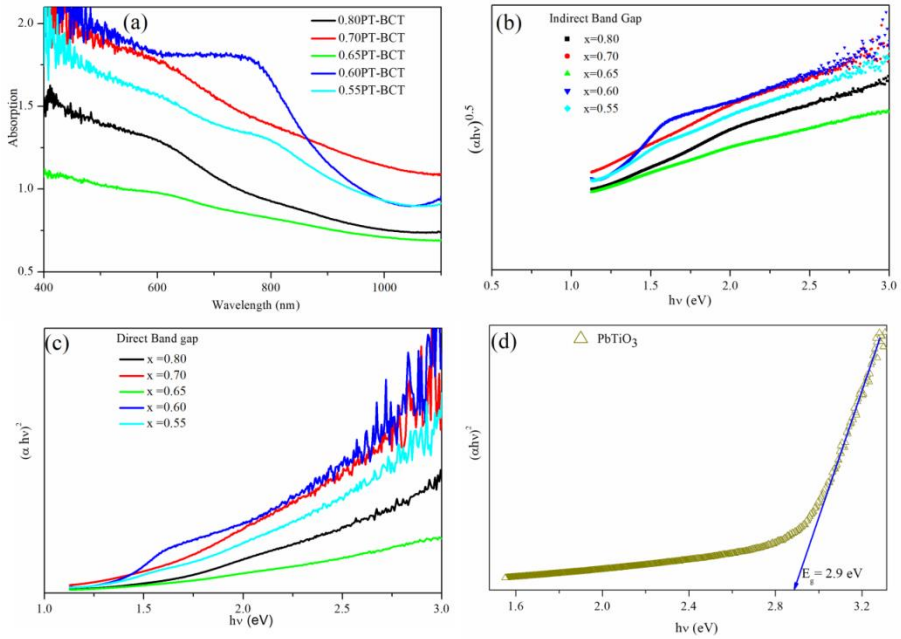

Figure 4.11 Composition dependent variations of (a) absorption spectra (b) Indirect band gap estimation plots using the Tauc equation $(\alpha h\upsilon)^{0.5}$ vs hυ (c) direct band gap estimation plots using the Tauc equation $(\alpha h\upsilon)^2$ vs hυ for $xPbTiO_3$-(1-x)$Bi(Co_{1/2}Ti_{1/2})O_3$ solid solution in the composition range ($0.80 \leq x \leq 0.55$) and (d) The Tauc plot $(\alpha h\upsilon)^2$ vs hυ for undoped $PbTiO_3$.

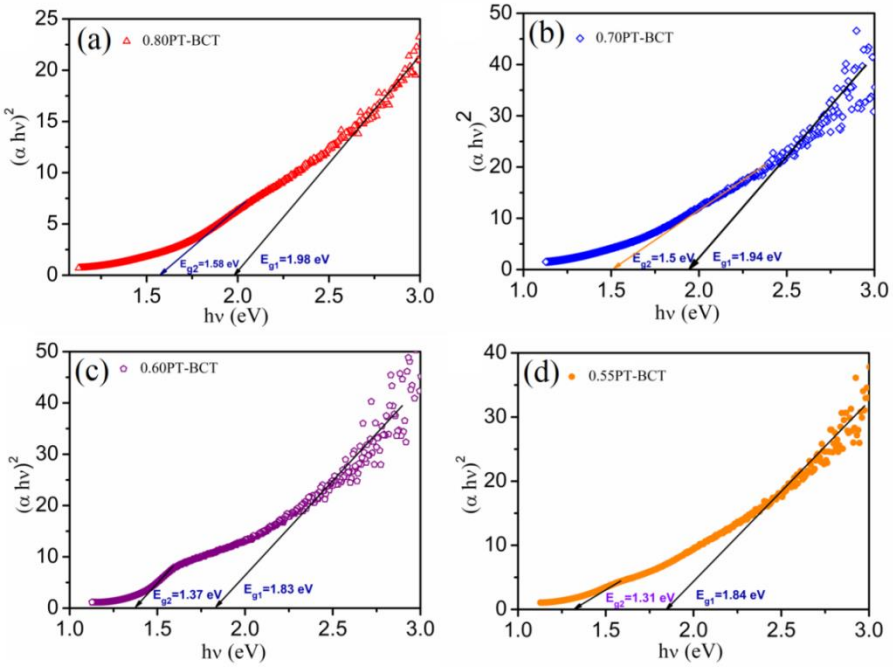

Figure 4.12 Composition dependent direct band gap estimation plots using the Tauc equation $(\alpha h\upsilon)^2$ vs hυ for $xPbTiO_3$-(1-x)$Bi(Co_{1/2}Ti_{1/2})O_3$ solid solution with compositions (a) x = 0.80 (b) x = 0.70 (c) x = 0.60 and (d) x = 0.55 respectively. The tangent line drawn for linear region is used to estimate the band gap.

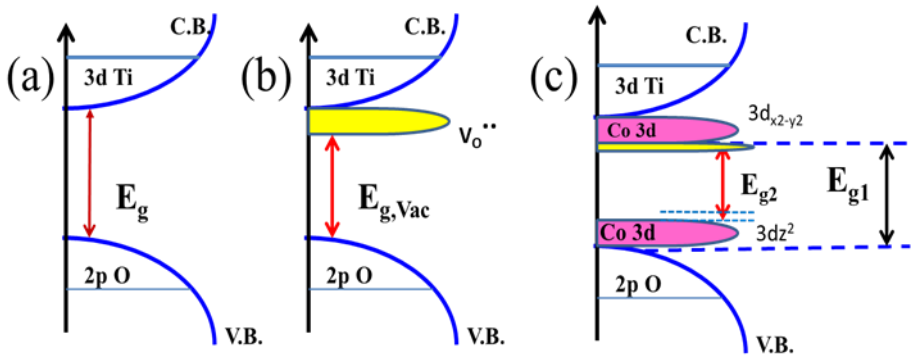

Figure 4.13 Schematic diagram of density of electronic states (a) Ideal situation for $PbTiO_3$ (b) With presence of oxygen vacancies (c) with presence of Co states and oxygen vacancies for $xPbTiO_3$-(1-x)$Bi(Co_{1/2}Ti_{1/2})O_3$.

4.3.4 The Band Gap Tuning by Changing Co/Ti ratio in $0.60PbTiO_3$-0.40Bi $(Co_yTi_{1-y})O_3$ Solid Solutions

As discussed in previous section, significantly lower bad gap is obtained for the $0.60PbTiO_3$-$0.40Bi(Co_{1/2}Ti_{1/2})O_3$ composition. Since Co-ion electronic states and oxygen vacancies states are crucial in reduction of band gap, we further optimized the Co/Ti ratio in $0.60PbTiO_3$-$0.40Bi(Co_yTi_{1-y})O_3$ solid solution to get the best band gap composition. Fig.4.14 shows the XRD patterns of $0.60PbTiO_3$-0.40Bi $(Co_yTi_{1-y})O_3$ solid solutions with varying the Co/Ti concentrations (y = 0.45, 0.50, 0.55, and 0.60). As can be seen from this figure, all the compositions exhibit major perovskite phase with tetragonal structure. The position of the x-ray diffraction peaks exhibits angular shift with changing Co concentration in 0.60PT-$0.40Bi(Co_yTi_{1-y})O_3$ indicating that Co/Ti ion concentration is successfully varying that causes lattice distortion. The increased 2θ separation in between (002), (200) peaks and (001), (100) diffraction peaks indicate an increase in tetragonality for higher Co-content. It may be attributed to the incorporation of the larger Co^{2+} cations (0.72Å) for smaller Ti^{4+}cations (0.68Å). In addition to the

perovskite phase, small fraction of secondary phase also appears for larger deviation of Co/Ti ratio due to un-compensated valency of B-site ion in BCT. The XRD peak near $2\theta = 27.9°$ is due to impurity Pb_3Bi_4-Ti_6O_{21} (JCPDS file no. 35-0007). However, the amount of impurity phase is so small that it has no impact on any functional properties being investigated in the present work.

The impact of varying Co/Ti ratio on the microstructure in $0.60PbTiO_3$-$0.40Bi(Co_yTi_{1-y})O_3$ ceramic was also investigated. The SEM images, shown in Fig 4.15, illustrate the surface morphology and EDS spectra of the $0.60PbTiO_3$-$0.40Bi(Co_yTi_{1-y})O_3$ solid solution with varying the Co/Ti concentration. It can be observed from inset of Fig 4.15 (b, d) that with increasing the Co content in $0.60PbTiO_3$-$0.40Bi$ $(Co_yTi_{1-y})O_3$, the particle size decreases from average size of 857 nm to 716 nm. Thus, higher Co^{2+} content is restricting the grain growth. The EDS spectra confirm the presence of Pb, Ti, Co, Bi and O elements only. Elemental mapping of $0.60PbTiO_3$-$0.40Bi$ $(Co_{0.50}Ti_{0.50})O_3$ solid solution and $0.60PbTiO_3$-$0.40Bi(Co_{0.60}Ti_{0.60})O_3$ solid solution is compared for Co distribution as shown in Fig 4.15 (c) and (d) . It is observed that Co is more densely distributed in $0.60PbTiO_3$-$0.40Bi$ $(Co_{0.60}Ti_{0.60})O_3$ solid solution.

The UV-visible absorption spectra of $0.60PbTiO_3$-$0.40Bi(Co_yTi_{1-y})O_3$ solid solutions with varying the Co/Ti concentration (y = 0.45, 0.50, 0.55, and 0.60) in the wavelength range of 400 nm-1100 nm is shown in Fig 4.16. The band gap decreases with increasing the Co concentration which is due to new states formed between conduction band minimum (CBM) and valance band maximum (VBM) as illustrated in Fig. 4.17 (a). The Co-3d-state is lower in energy than the Ti-3d states which increases the tailing of conduction band edge and thus reduces the band gap as illustrated in Fig 4.17. According to previous studies [R. E. Cohen et al. (1992)], the conduction band minimum (CBM) and valence band maximum (VBM) of $PbTiO_3$ are occupied by Pb-6p

Ti-4d and O-2p orbitals. In PT-BCT Co-3d and O-2p orbitals form the top of the valence band while bottom of the conduction band comprises Co-3d, Bi-6p and O-2p orbitals [E. Mete et al. (2019)]. For the density of electronic states of PT-BCT, the band gap is decreased than $PbTiO_3$ due to Pb_{Bi} and Ti_{Co} substitution. Ti_{Co} creates a new localized band below the conduction band minimum as mentioned in Fig. 4.17 [Z. Pan et al (2017), B. S. Holinsworth et al. (2015)].

As mentioned in section 4.3.3, it is experimentally observed that appropriate BCT doping decreases the band gap of $PbTiO_3$ which further reduced by changing the stoichiometric ratio of Co/Ti in 0.60PT-0.40BCT. The change in stoichiometric ratio of Co and Ti of 0.60PT-0.40BCT with increased Co also increases the oxygen vacancies to compensate for the valance as Co is divalent while Ti is tetravalent ion. The formation energies for oxygen vacancy at the sites around Co atoms are smaller than those around Ti atoms. The increased number of oxygen vacancies due to higher Co doping creates defect levels in the forbidden band which further reduces the band gap as illustrated schematically in Fig 4.17. So, further lowering of band gap of PT-BCT can be attributed to increased Co^{2+} doping than Ti-content in BCT. The lowest band gap (E_{g1} = 1.65 eV) is obtained for $0.60PbTiO_3$-$0.40Bi(Co_yTi_{1-y})O_3$ (y = 0.60) which is suitable to absorb the visible light and thus it could be a potential photoactive material for perovskite based ferroelectric photovoltaic devices.

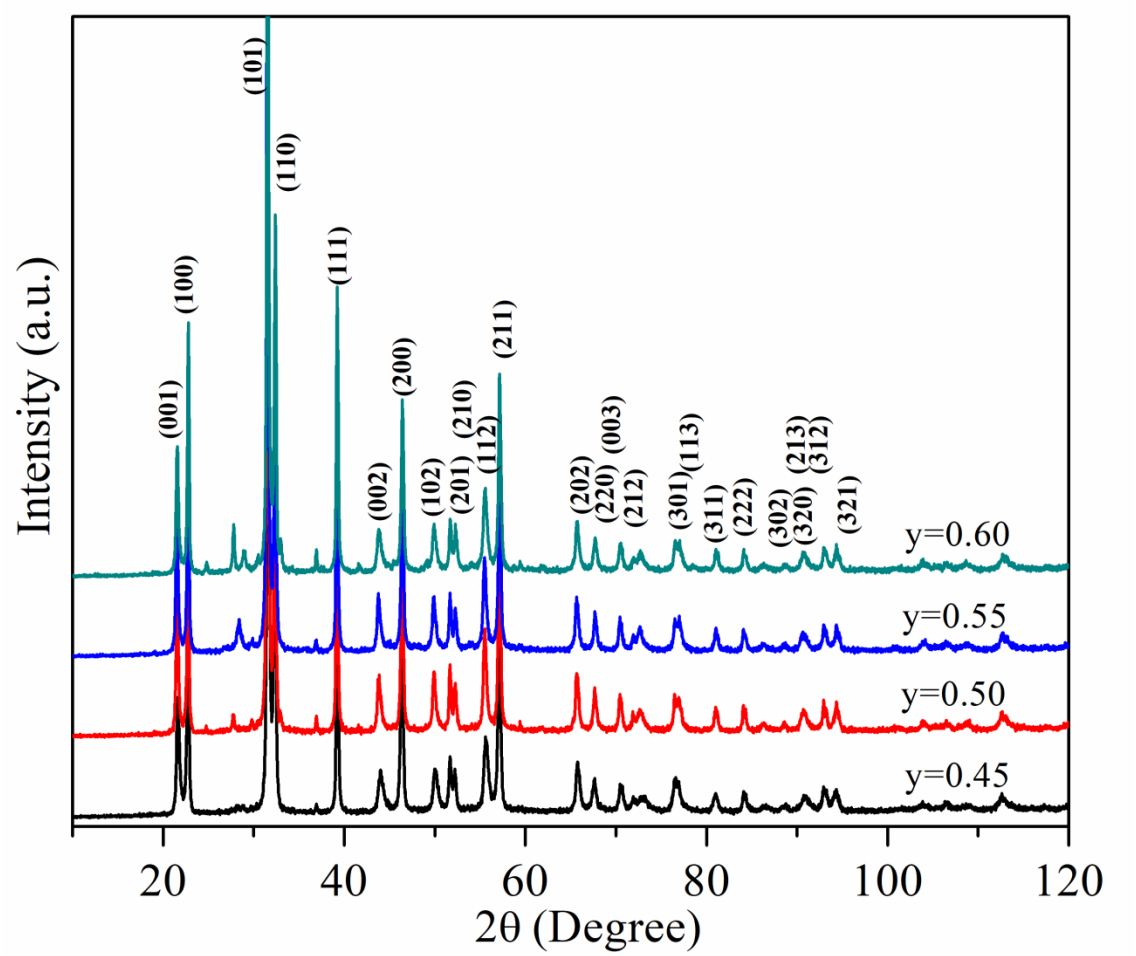

Figure 4.14 Powder x-ray diffraction patterns of $0.60PbTiO_3$-$0.40Bi(Co_yTi_{1-y})O_3$ with varying Co/Ti concentration, y=0.45, 0.50, 0.55 and 0.60.

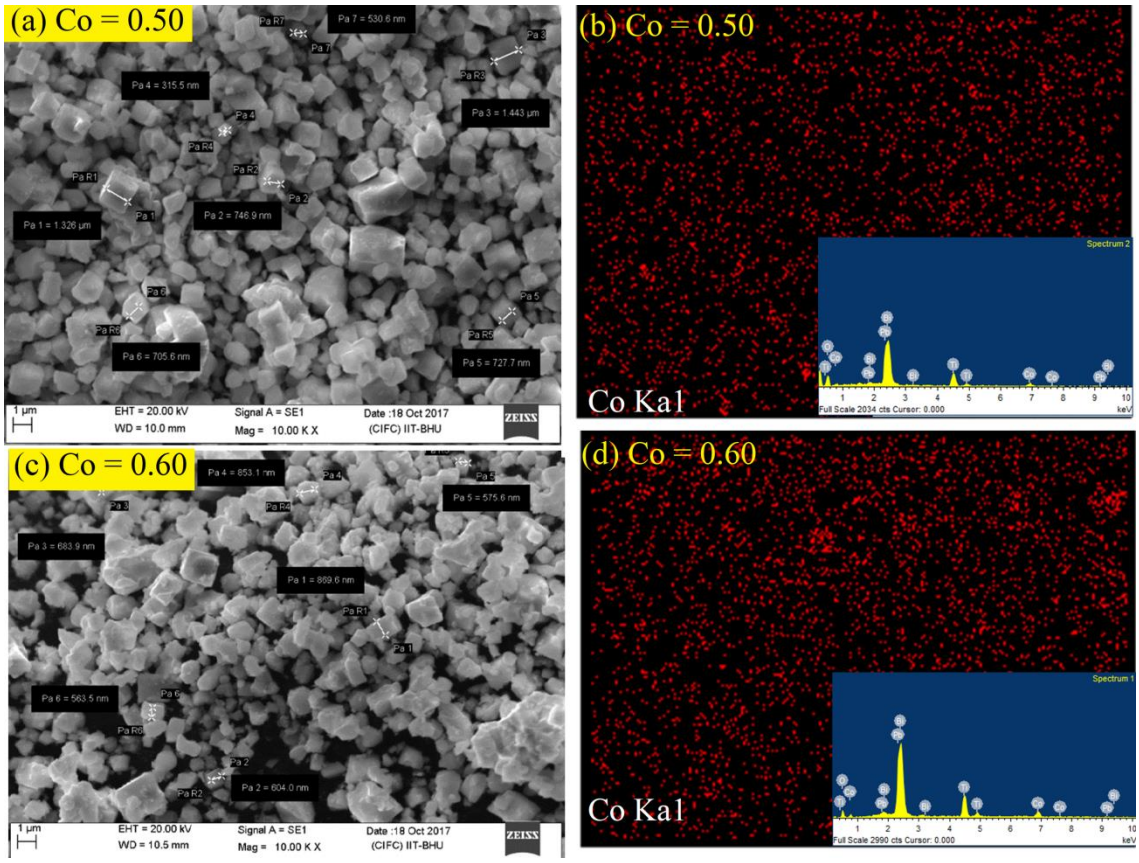

Figure 4.15 SEM Image of $0.60PbTiO_3$-$0.40Bi(Co_yTi_{1-y})O_3$ solid solution with composition (a) y=0.50 and (c) 0.60 and Elemental mapping of Co in $0.60PbTiO_3$-$0.40Bi(Co_yTi_{1-y})O_3$ sample with composition (b) y = 0.50 and (d) y = 0.60. In inset, respective EDS spectra is shown.

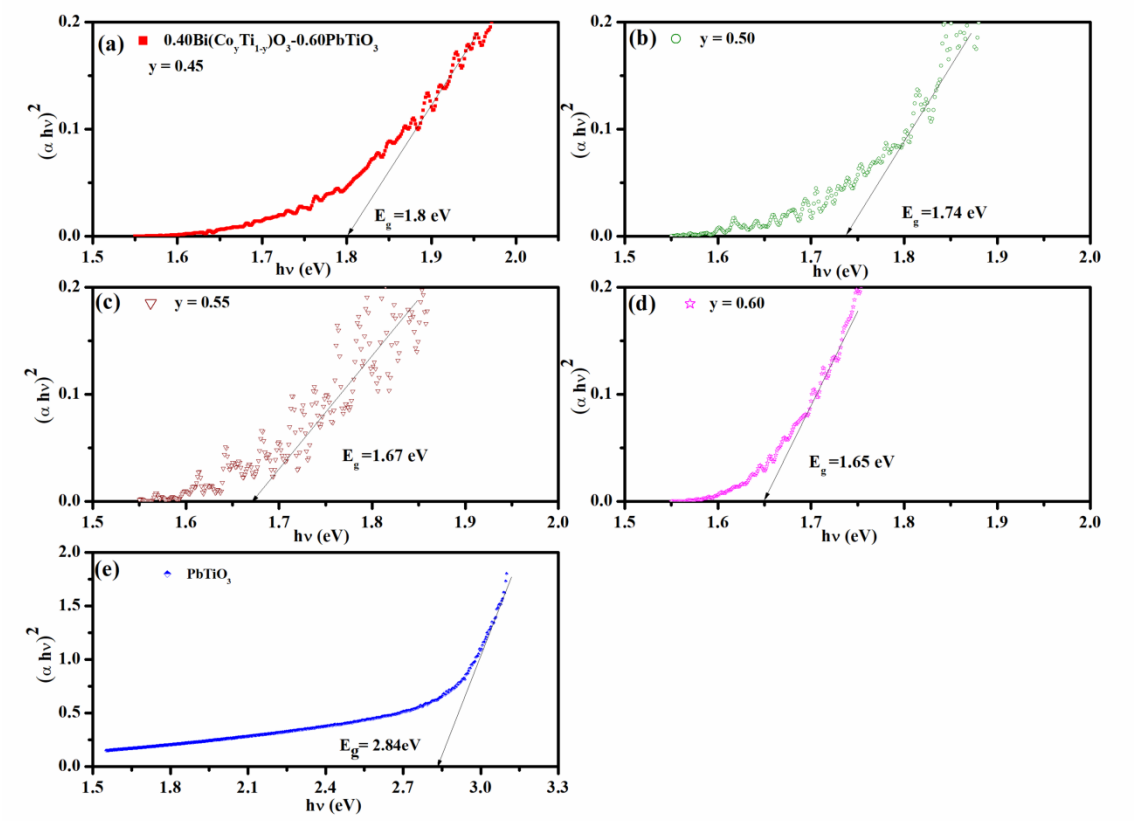

Figure 4.16 The Tauc equation $(\alpha h\upsilon)^2$ vs hυ plots for $0.60PbTiO_3$-$0.40Bi(Co_yTi_{1-y})O_3$ solid solution with composition (a) y=0.45 and (b) 0.50 (c) 0.55 and (d) 0.60. The tangent line extrapolation on the linear region is used to estimate the band gap.

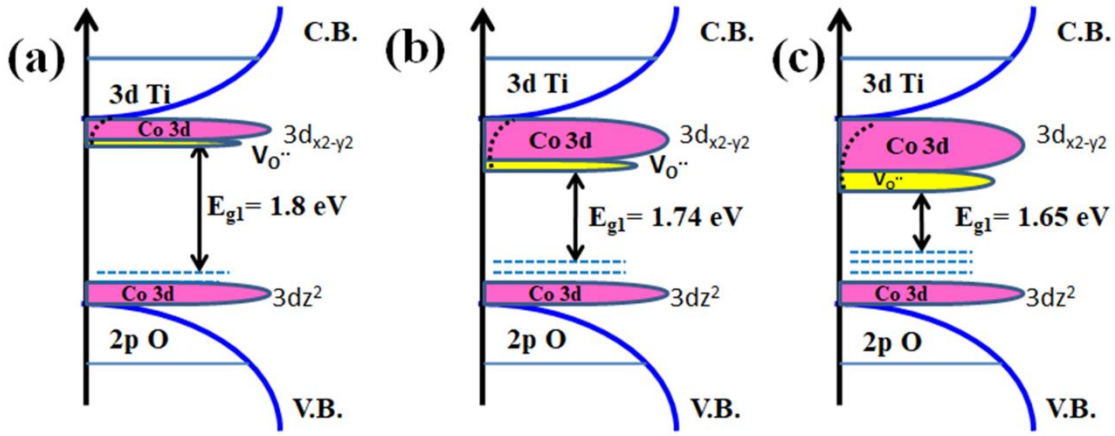

Figure 4.17 Schematic diagram of density of electronic states for $0.60PbTiO_3$-$0.40Bi(Co_yTi_{1-y})O_3$ solid solution with composition (a) y=0.45 and (b) 0.50 (c) 0.60. The increasing CBM tailing is shown by dotted lines and states created by oxygen vacancies are drawn in yellow colour area.

4.3.5 Fabrication of $0.60PbTiO_3$-$0.40Bi(Co_{0.60}Ti_{0.40})O_3$ Thin Films and Their photoelectrical properties

As discussed in previous section, the lowest band gap (E_{g1} = 1.65 eV) is obtained for $0.60PbTiO_3$-$0.40Bi(Co_yTi_{1-y})O_3$ (y=0.60) composition. The properties for this composition were further investigated by preparing sample in thin film form. Polycrystalline $0.60PbTiO_3$-$0.40Bi(Co_{0.60}Ti_{0.40})O_3$ (PT-BCT) thin films were deposited on FTO coated glass substrates using a two inch diameter target of the ceramic sample with RF-magnetron sputtering. As deposited films, were further annealed at 600°C for an hour in furnace to ensure better crystallization. In the XRD characterization, the diffraction pattern of PT-BCT sputtering target is collected and compared with the XRD pattern of magnetron sputtered PT-BCT thin film as shown in Fig. 4.18 (a). Film deposited at 300°C substrate temperature shows amorphous nature and no perovskite phase is observed. When film is annealed at 600°C in O_2 atmosphere, the diffraction peaks are observed in XRD pattern which are matching with perovskite phase.

The surface SEM image of PT-BCT thin film is shown in Fig. 4.18 (b). Film is compact, crack-free, well crystallized and have dense microstructure. Fig. 4.19 shows the cross-section image of PT-BCT thin film deposited on FTO coated glass substrate. The thickness of PT-BCT film is around 345 nm as depicted in Fig. 4.19. The thickness of bottom electrode FTO is around 532 nm. Inset of Fig. 4.19 is showing the EDS spectra of as deposited PT-BCT film. The EDS spectra confirm the presence of Pb, Ti, Co, Bi and O elements only in magnetron sputtered PT-BCT thin film.

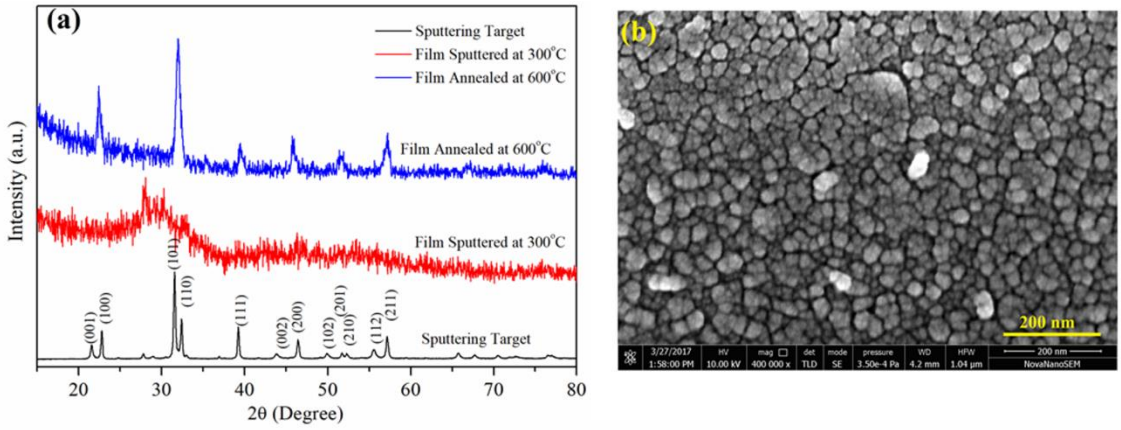

FIGURE 4.18 (a) XRD pattern (b) SEM image of as deposited PT-BCT thin films.

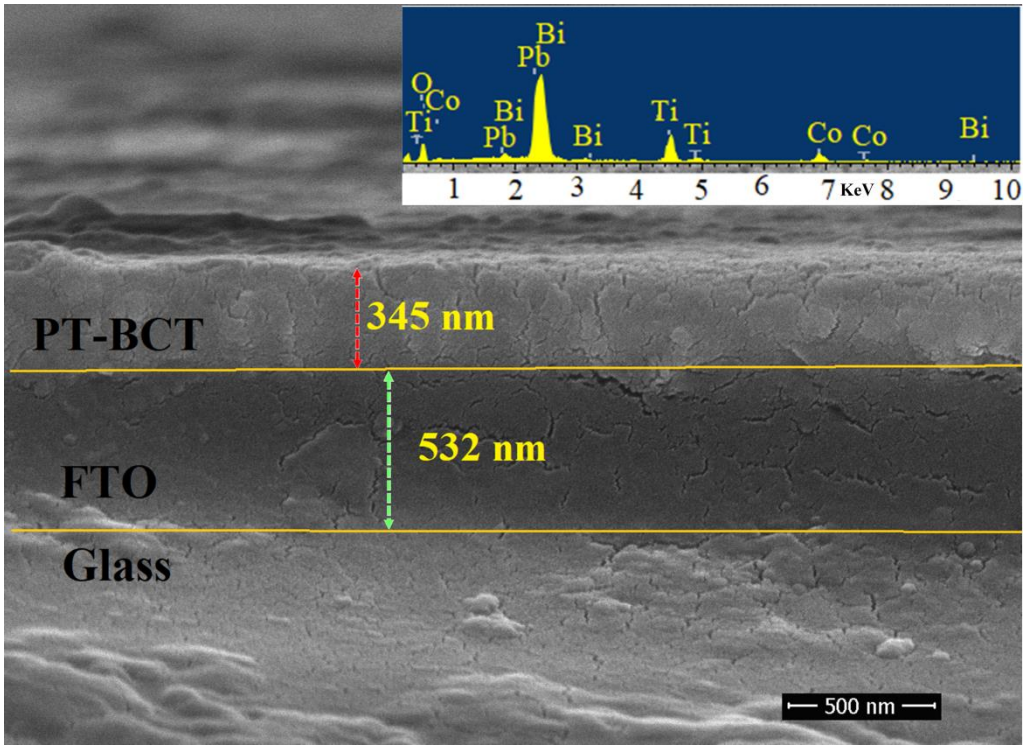

FIGURE 4.19 Cross-section SEM image of as deposited PT-BCT thin film on FTO glass Substrate. Inset is showing EDX spectra of PT-BCT film.

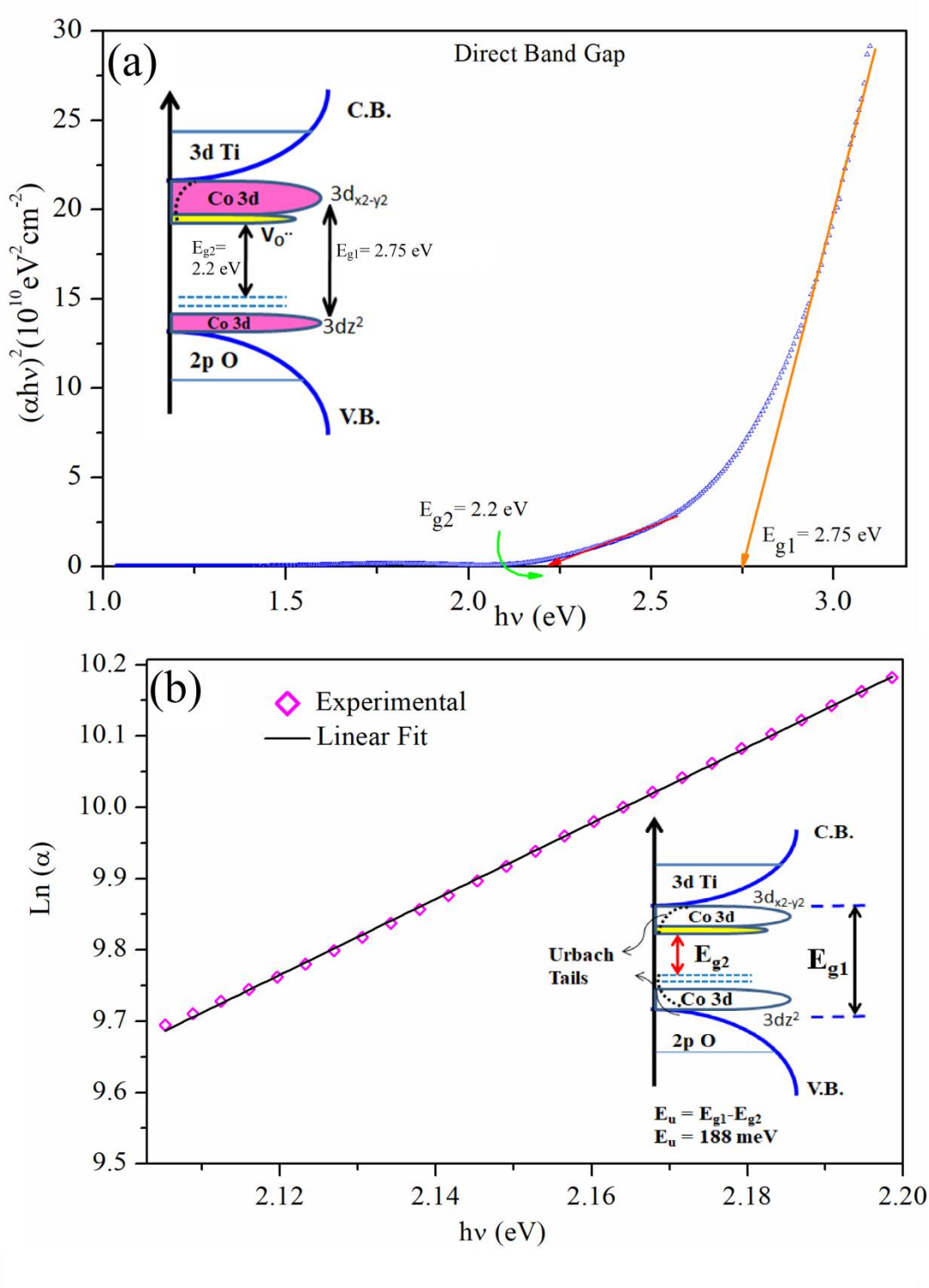

FIGURE 4.20 (a) Tauc plots and band gap (b) Urbach Energy of as deposited PT-BCT thin films.

4.3.6 Optical Properties of $0.60PbTiO_3$-$0.40Bi(Co_{0.60}Ti_{0.40})O_3$ Thin Film

The UV-visible absorption data of as deposited PT-BCT film is collected and used to calculate the optical band gap by Tauc's equation [J. Tauc (1970)]. Fig. 4.20 (a) shows the $(\alpha h\upsilon)^2$ vs hυ plot. By extrapolating the linear portion of Tauc's plot to zero, the optical band gap (E_{g1}~ 2.7 eV) was obtained as shown in Fig. 4.20 (a). In low energy portion of $(\alpha h\upsilon)^2$ vs hυ plot, one more region is linear which shows a band gap (E_{g2}) value of 2.2 eV. The obtained band gap values of magnetron sputtered PT-BCT films is lower than $(1\text{-}x)PbMg_{1/3}Nb_{2/3}O_3$-$xPbTiO_3$ perovskite thin film grown by pulsed laser deposition [K. Y. Chen et al. (2004)]. This second band gap may be due to presence of oxygen vacancies. The observed lower band gap in PT-BCT thin film is explained by energy band diagram shown in inset of Fig. 4.20 (a). The sub-bands created due to oxygen vacancies and Co doping extends the CBM tail and thus lowers the band gap. Due to presence of Co ions and O_2^- vacancies, additional localized sub-bands states are created below conduction band. The oxygen vacancies and structural defects further created defect states below C.B. and experimentally another band gap (E_{g2} ~ 2.2 eV) is obtained in low energy region. These defect states are confirmed by measuring the Urbach energy. The Urbach energy value presents the width of the tail of sub-band states created between conduction band and valence band. These sub-band states trap the excited electrons before it reach to conduction band and cause absorption tail in the absorption spectra [Z. Sun et al. (2021)]. The absorption coefficient (α) is related to Urbach energy (E_u) as presented in equation $\alpha = \alpha_0 \exp(h\upsilon/E_u)$ [F. Urbach (1953)]. Fig. 4.20 (b) shows the ln (α) vs hυ plot and linear fitting provide the Urbach energy 188 meV. The Urbach energy value indicates the amount of oxygen vacancies and defects in PT-BCT films. The vacancies created due to Co doping and structural defects during film growth affect the optical absorption of PT-BCT film [V. Bhavanasi et al. (2013)].

These vacancies and defects created new sub-band states below CBM and cause broadening of conduction and valence band. The inset of Fig, 4.20 (b) shows the schematic diagram of energy states which shows the position of Urbach tails. The high value of Urbach energy indicates that Co 3d states creates midgap states bellow conduction band and also above the valence band [S. Das et al. (2018)].

4.3.7 Study of Nano-scale ferroelectric phenomenon

We have investigated the ferroelectric features of $0.60PbTiO_3$-$0.40Bi(Co_{0.60}Ti_{0.40})O_3$ films at nanoscale using combination of atomic force microscopy (AFM) and piezo-force microscopy (PFM). To characterize the surface of film, 5µm-5µm area of film was scanned. Fig. 4.21 (a) shows the surface topography and Fig. 4.21 (b) shows the distribution of grains for the thin film sample of $0.60PbTiO_3$-$0.40Bi(Co_{0.60}Ti_{0.40})O_3$. The 3-D microstructure of the film is shown in Fig. 4.21 (c) and roughness profile is shown in Fig 4.21 (d). The root-mean-square (rms) roughness of the film is determined to be around 24 nm. The grain sizes are in the range of 0.1 µm -0.6 µm and most of the grains are of 0.2 µm size.

The local ferroelectric properties were investigated by PFM. The ferroelectric domain imaging of $0.60PbTiO_3$-$0.40Bi(Co_{0.60}Ti_{0.40})O_3$ film at nanometer scale and local switching are shown in Fig. 4.22. The PFM images of the samples, poled with (-10V), unpoled, and poled with +10V, are presented in Fig. 4.22 a, b, and c, respectively. The domains are seen to be partially switched by applying ±10V dc voltage pulse. The resulting contrast confirms the ferroelectricity at nanoscale in $0.60PbTiO_3$-$0.40Bi(Co_{0.60}Ti_{0.40})O_3$ thin film. Fig 4.22 shows the topography and the corresponding PFM amplitude and phase image of PT-BCT film with and without poling. The topography image shows films with grains. As shown in Fig 4.22 (c) and Fig. 4.22 (i) , the ferroelectric switching characteristics for +ve poled and –ve poled samples are

different. The PFM results confirm the polarization charge in PT-BCT film at nanoscale. Fig 4.23 (b) and Fig 4.23 (d) shows the section profile of topography and PFM phase respectively which tells about grain boundaries and position of domain walls.

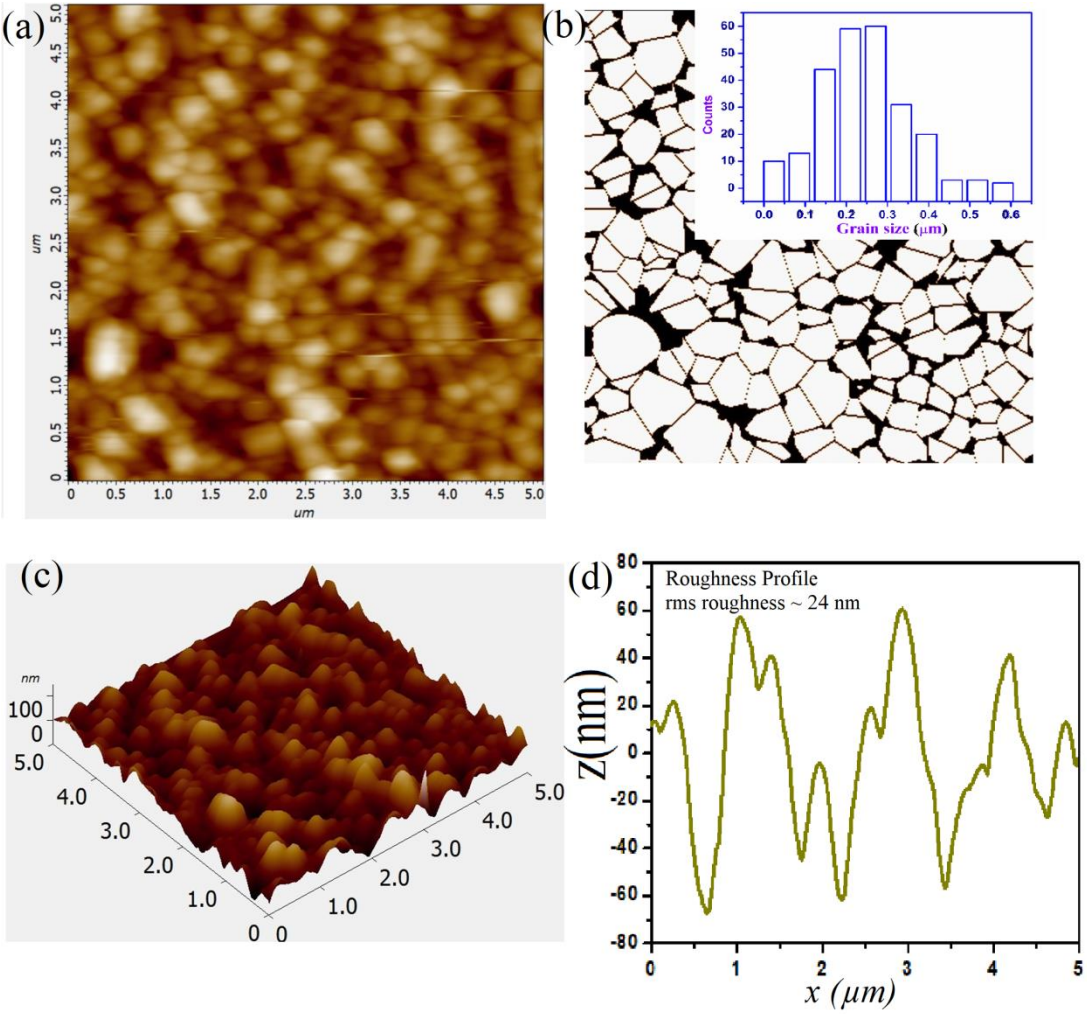

Figure 4.21 (a) AFM topography image, (b) grain size distribution obtained from AFM image and corresponding histogram (c) 3-D microstructure (d) AFM roughness profile for $0.60PbTiO_3$-$0.40Bi(Co_{0.60}Ti_{0.40})O_3$ thin film.

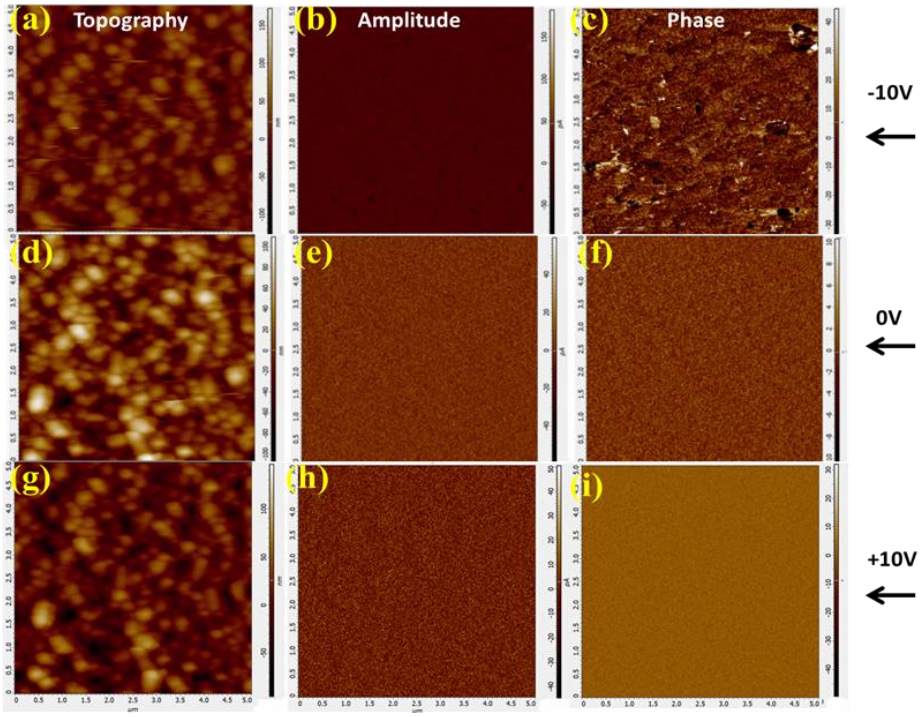

Figure 4.22 AFM/PFM images for $0.60PbTiO_3$-$0.40Bi(Co_{0.60}Ti_{0.40})O_3$ thin film, (a) AFM topography image, (b) PFM Amplitude and (c) PFM Phase image for negatively poled film; (d) Topography, (E) PFM amplitude and (f) PFM phase image for unpoled film; (g) Topography (b) PFM Amplitude and (c) PFM Phase image for positively poled film.

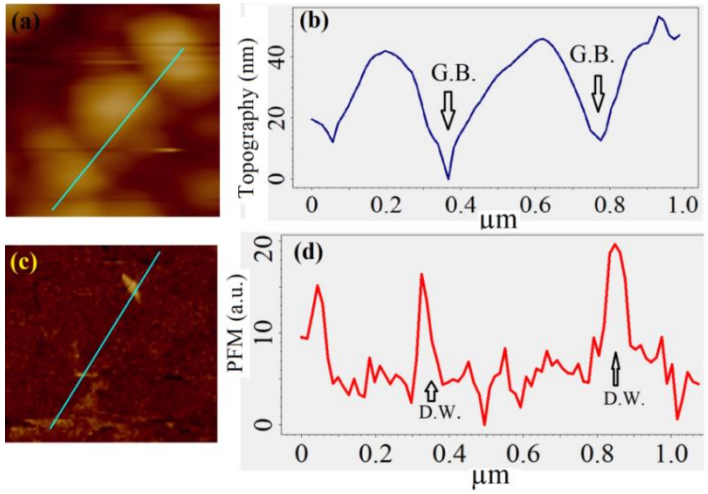

Figure 4.23 (a) AFM topography image and corresponding (b) Cross section profile which is showing grain boundaries (G.B.); (c) PFM phase image and their (b) Cross section profile which is showing domain walls (D.W.); for $0.60PbTiO_3$-$0.40Bi(Co_{0.60}Ti_{0.40})O_3$ thin film. The arrows are used to indicate the position of D.W. and G.B. in profile image.

4.3.8 Current-Voltage (I-V) Characteristics and Conduction mechanism study of Ag/0.60$PbTiO_3$-0.40$Bi(Co_{0.60}Ti_{0.40})O_3$/FTO device

For device fabrication, Ag thin film was deposited on 0.60$PbTiO_3$-0.40$Bi(Co_{0.60}Ti_{0.40})O_3$ thin film by vacuum evaporation method using a shadow mask. The current-voltage (I-V) characteristics of as prepared Ag/0.60$PbTiO_3$-0.40$Bi(Co_{0.60}Ti_{0.40})O_3$/FTO device (now onward designated as Ag/PT-BCT/FTO device) was measured by using electrometer in dark and under light illumination under zero external bias voltage. Since, the band gap of 0.60$PbTiO_3$-0.40$Bi(Co_{0.60}Ti_{0.40})O_3$ (PT-BCT) is 1.65 eV, the photons having wavelength less than 677 nm can only stimulate the electron-hole pairs in device. For light illumination, green laser (λ = 532 nm) light with power of 5 mW to 50 mW and visible light (100 mW) were used. Fig. 4.24 shows the photo-response of Ag/PTBCT/FTO heterostructure upon light switching ON and switching OFF. When light incident on PTBCT surface the electron-hole pairs are generated and can be described by equation $h\nu \rightarrow e^- + h^+$, after separation photo-generated charge carriers, holes transported towards surface and recombine with O_2^- ion. In this process ($O_2^- + h^+ \rightarrow O_2$ (g)), the unpaired electrons accumulate gradually with time until the desorption and readsorption of oxygen attain an equilibrium state. This accumulation of electrons will increase the conductivity of surface and also increase the photocurrent till a saturation reached [J. Zhou et al. (2009)].

Fig. 4.25 shows J-V curves of Ag/PT-BCT/FTO device in dark and under light illumination. A clear rectifying behaviour was seen for the device. From these J-V curves, a short-circuit current density (J_{sc}) of 0.325 $\mu A/cm^2$ and open-circuit voltage (V_{oc}) of 0.09 V were obtained for the fabricated device. The photovoltaic mechanism under zero external bias voltage can be explained by using energy level diagram of Ag/PT-BCT/FTO heterostructure with the help of previously reported energy level

parameters as shown in Fig 4.26. When light is illuminated on FTO bottom side, the electronic charges are generated in the PT-BCT layer. The internal electric field in ferroelectric PT-BCT layer separates the photo-generated electronic charge carriers. Then, the electrons from the PT-BCT layer are transferred to the FTO electrode and holes are transferred to Ag-electrode. The transportation of electrons and holes gives rise to a photocurrent at zero external bias voltage.

The low V_{oc} in Ag/PT-BCT/FTO device may be due to unpoled PT-BCT layer. In unpoled devices, the net built-in field depends on top and bottom Schottky barrier difference. In this work, Ag/PT-BCT/FTO devices have two interfaces: Ag/PT-BCT and PT-BCT/FTO. Based on previous reports, the electron affinity of FTO is 4.7 eV and work function of Ag is 4.5 eV, these earlier reported values are considered to calculate the internal net potential. The built–in-field in the device is due to the presence of different electrode materials and value is nearly -0.2 eV. The Schottky barrier difference for polycrystalline ferroelectric films are usually lower than the theoretical values [M. Qin (2009)]. As samples are unpoled, so depolarization field is not active. The obtained low V_{oc} (~0.09 V) is reasonable for this type of device structure.

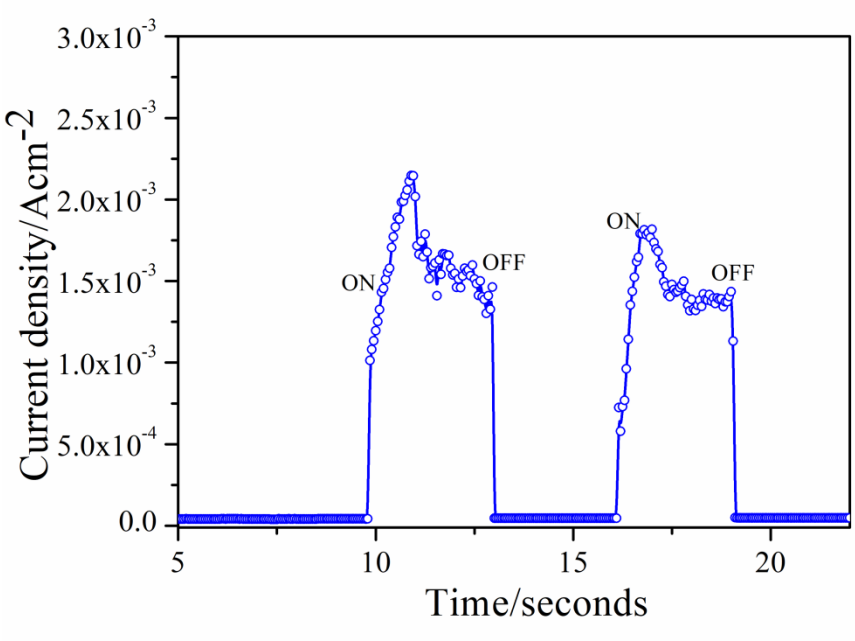

Figure 4.24 Time dependent photocurrent response of Ag/PTBCT/FTO device under light illumination.

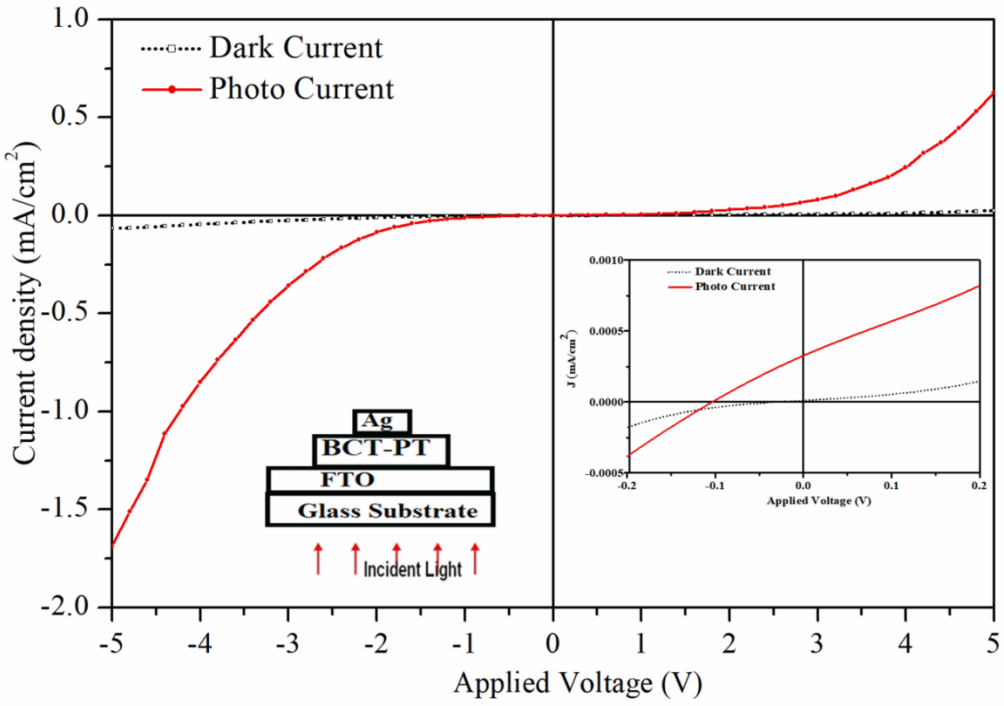

Figure 4.25 J-V characteristics of Ag/PT-BCT/FTO heterojunction in dark and light illumination. The Inset shows same graph as the semi-log J-V plot.

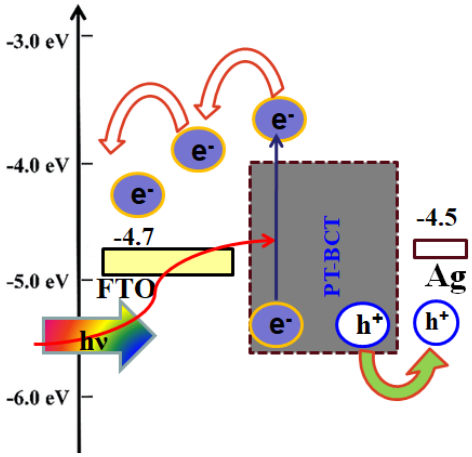

Figure 4.26 A schematic energy level diagram for Ag/PT-BCT/FTO Heterostructure showing the internal photo-electric process.

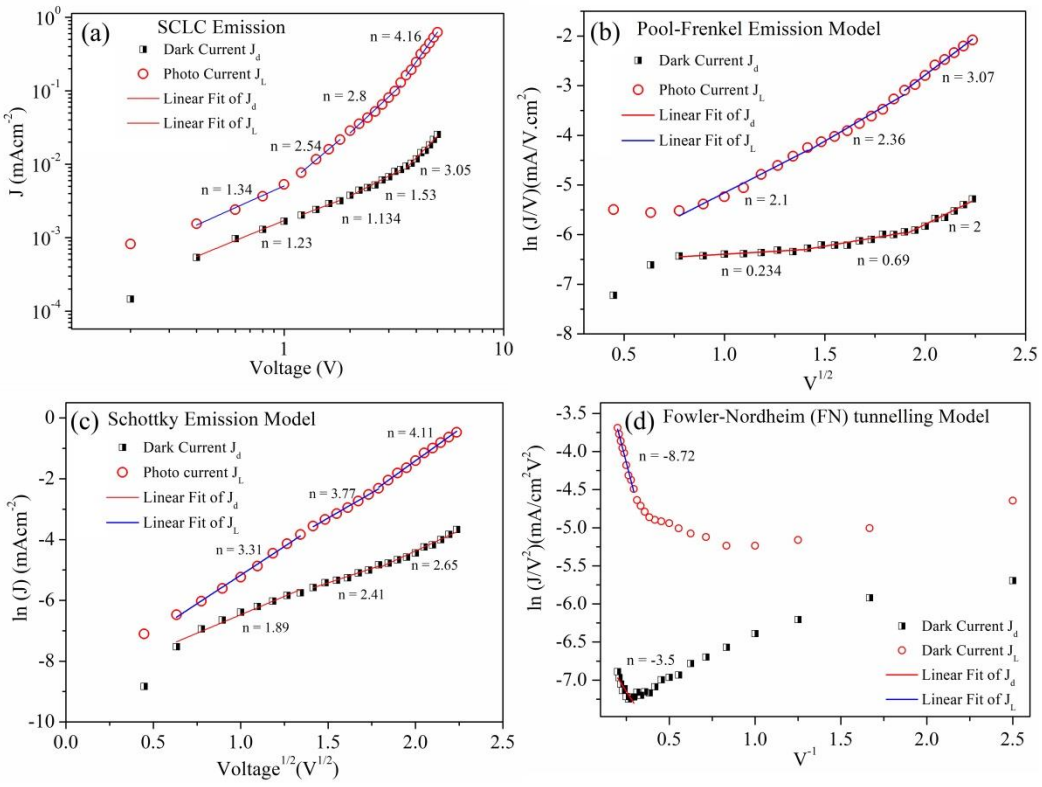

FIGURE 4.27 Typical time-zero current-voltage data and various fits of data to determine the conduction mechanism in Ag/PT-BCT/FTO heterostructure (a) Space-charge-limited conduction (SCLC), (b) Poole-Frenkel (PF) emission, (c) Schottky Emission model, and (d) Fowler-Nordheim (F-N) tunneling.

In order to get more insight into transport behaviour of carriers, electrical conduction mechanism of Ag/PT-BCT/FTO is investigated and four possible conduction mechanisms have been discussed. The measured current behaviour cannot be explained by a single mechanism as conduction mechanism depends on structural, morphological and interface near electrode. So, different mechanisms exist at different applied field range. The conduction mechanisms can be divided in two parts bulk limited conduction mechanism [space-charge-limited conduction (SCLC) and Poole-Frenkel (PF) emission] and interface-limited conduction mechanisms [Schottky emission (SE) and Fowler-Nordheim (FN) tunneling] [Z. X. Li et al. (2014); F. Chiu (2014)]. The obtained I-V curve is asymmetric type so both bulk and interface conduction models are used to analyze and compare the conduction mechanism to know their relative contribution. We will identify the charge transport mechanism after fitting the above discussed model. According to SCLC model [N. F. Mott et al. (1948)] the current density is expressed as

$$J_{SCLC} = \frac{9}{8}\theta_f \mu \varepsilon_r \varepsilon_0 \frac{V^2}{L^3} \tag{4.1}$$

Where θ_f is the fraction of injected carriers, ε_r is dielectric constant of film, μ is the charge carrier mobility and L is the film thickness. In SCLC model, it is assumed that the charge carriers are travelling through the film thickness and current is according to ($J \propto V^n$) with $n \geq 2$ [N. F. Mott et al. (1979)]. Fig 4.27 (a) shows the ln J versus ln V plot. There are four linear regions are observed in ln J vs ln V curve. The SCLC behaviour provides information about traps in film. The oxygen vacancies in PT-BCT films create defects which form the electron traps. In the voltage range ($0.4 < V < 3.44$) , the slop of linear region is less than 1.5 for dark current which indicate that this region is Ohmic region. When applied voltage is less than 1.0 V, both dark and photocurrent

controlled by traps in film and thermally generated charge carriers are more than the injected charge carriers [A. Bogusz et al. (2016)]. The photocurrent in its intermediate voltage range (1.2 < V < 3.44), have slope (n > 2), indicate that charge transport mechanism is combination of SCLC behaviour and trap-filled process [G. R. Fox et al. (1993)]. In voltage range (1.2 < V < 3.44), the injected carriers dominate over the thermally generated charge carriers. In higher voltage range (more than 3.5 V) the slop is around 4.16 which indicate that the trap inside the material begin to be filled with injected charge carriers. The presence of several linear regions in ln J versus ln V plot is also reported for $BiFeO_3$ by J. Wu et al. [J. Wu et al. (2010)]. Only intermediate region of lnJ - lnV curve is follow SCLC mechanism, so for analyzing the current in higher applied voltage region Poole-Frenkel emission model is applied. In PF emission, the conduction process is primarily driven by thermally released charge carriers from trapped centers under strong electric field [H. Schroeder (2015)]. According to PF emission model current density is

$$J_{PF} = DVexp\left(\frac{-E_i+\sqrt{q^3V/\pi\varepsilon_0\varepsilon_r L}}{k_B T}\right) \quad (4.2)$$

Where D is constant, V is applied voltage, q is the elementary charge, E_i is the trap ionization energy, L is the film thickness and ε_r is the relative dielectric constant. The physical basis for existence of PF mechanism is the thermal emission of electrons from Columbic traps to conduction band enhanced by the applied voltage [L. Maissel (1970)]. The curve between ln (J/V) versus $V^{1/2}$ should have linear region for PF emission mechanism. For dark current, the linear region is found at high applied voltage but no reasonable linear fitting is obtained at lower applied voltage range as shown in Fig. 4.27 (b). Under dark condition, curve slope is less than 1 in range 0.6 < V < 2 which confirms the experimentally observed low current due to slow movement of

charge carriers and low density of charge carriers as they are controlled by the traps. The photocurrent have linear region with slope more than 2.

The Schottky emission conduction model is used to analyse the Schottky potential barrier at PT-BCT/Ag interface. Schottky emission is an interface limited emission which is caused by a difference in Fermi levels between a metal electrode and semiconductor or insulating layer [G. W. Pabst et al. (2007), A.Z. Simões et al. (2011)] J-V data is fitted by using the SE model according to the following equation:

$$J_{SE} = A^{*}T^{2} \exp\left(\frac{-\left(\Phi_B - \sqrt{q3V/4\pi\varepsilon_0\,\varepsilon_{opt}\,L}\right)}{kT}\right) \quad (4.3)$$

Where J is the current density, A^{*} is the Richardson constant, T is the temperature, q is the electronic charge, Φ_B is height of the Schottky barrier at 0 V, V is applied voltage, k is the Boltzmann constant, L is film thickness, ε_0 is the permittivity of free space and ε_{opt} is the optical dielectric permittivity respectively. Figure 4.27 (c) show the ln (J) versus $V^{1/2}$ characteristics of PT-BCT film according to Schottky emission where linear behaviour is observed for photocurrent. Under dark condition, ln (J) versus $V^{1/2}$ curve slope is nearly 2, linear region is observed only in limited range $0.38 < V < 3.2$. In this region it follows Child's law. In region $2< V < 5$, slope is more than 2 and it follows the power law. Under light condition, ln (J) versus $V^{1/2}$ curve, the slope is more than 3 and we can conclude that the injection of charge carriers through traps from PT-BCT is enhanced because of incident light effect and applied voltage. The slope more than 2 may be due to traps and presence of built-in-voltage.

The electrode-dielectric interface may also have contribution in conduction mechanism. The Fowler-Nordheim (FN) tunnelling model is used to study the possible charge injection process during conduction mechanism [C. P. Perkins et al. (2018)]. In FN

tunnelling mechanism, it is assumed that charge carriers tunnel directly in to the bands of the dielectric layer [R. H. Fowler et al. (1928), T. Ikuno et al. (2011)]. In Fowler-Nordheim (FN) tunnelling, current density as a function of applied voltage could be expressed as

$$J_{FN} = BV^2 \, exp\left(-\frac{C\Phi_i^{3/2}}{V}\right) \tag{4.4}$$

Where B and C are the constants, Φ_i is the potential barrier height and V is the applied voltage [S. M. Sze (1981)]. The FN tunneling model is used to find out the interface based conduction mechanism where the ln (J/V^2) versus (V^{-1}) plot should have linear region with a negative slope. Figure 4.27 (d) shows the ln (J/V^2) versus (V^{-1}) curve which is used to find out the presence of FN tunneling in PT-BCT films. Figure 4.27 (d) shows negative slopes of -3.5 for linear region of dark current and -8.72 for linear region of photocurrent in high voltage region ($3 < V < 5.0$). The observed negative slopes in ln (J/V^2) versus (V^{-1}) curve indicate the formation of a partial depletion layer between the thin film and the electrode. The inflection point is at 1.5 V for photocurrent and at 3.26 V for dark current. So, it can be possible that FN tunnelling mechanism is also play an important role in charge transport. The non-linearity in ln (J/V^2) versus (V^{-1}) curve for dark current may be due to contribution of space charge limited conduction, trap-filled limited conduction and thermionic emission current. So, we can say that photocurrent is also governed by FN tunneling mechanism [X. Yan et al. (2015)]. So, we can conclude that SCLC and Schottky mechanism dominates the charge transport mechanism in PT-BCT films and FN tunneling and PF emissions have also small contribution at higher applied voltage.

The solar cell device efficiency depends on various factors, so, to enhance the device efficiency, it is useful to study key parameters which affect the solar cell performance.

In order to extract the Schottky diode parameters from I-V data of Ag/PT-BCT/FTO capacitor, thermionic emission theory is applied. The parameters like saturation current density (J_0), ideality factor (η), charge mobility (μ) and barrier potential (Φ_B) are extracted using R-S thermionic emission model from current-density-voltage (J-V) curve [E. H. Rhoderick et al. (1988); V. Mikhelashvili et al. (2001)]. The relation between current and applied voltage for ideal diode can be expressed as

$$J = A^* T^2 exp\left(\frac{-q\Phi_B}{kT}\right) exp\left(\frac{qV}{kT} - 1\right) \quad (4.5)$$

$$J = J_0\left(exp\left(\frac{qV}{kT}\right) - 1\right) \quad (4.6)$$

Where J_0 is $J_0 = A^* T^2 exp\left(\frac{-q\Phi_B}{kT}\right)$

For V> 3kT/q, $$J = J_0\left(exp\left(\frac{qV}{kT}\right)\right) \quad (4.7)$$

Taking into account the non-ideal behaviour of a practical diode, a dimensionless parameter η is included in equation 4.7 [S. M. Sze (2007)]

$$J = J_0\left(exp\left(\frac{qV}{\eta kT}\right)\right) \quad (4.8)$$

Where J is the current density, J_0 is the dark saturation current density, η is the ideality factor, k is the Boltzmann's constant, T is the absolute temperature in kelvin and q is the elementary charge. Equation 4.8 can be written as

$$\log J = \log J_0 + \frac{qV}{2.303\eta kT} \quad (4.9)$$

$$\log J = \log J_0 + \frac{V}{2.303\eta V_T} \quad (4.10)$$

Where V_T = kT/q =25.85 meV, plot log J vs V, should be linear and this linear region will provide the ideality factor 'η' from slope

$$\eta = \frac{1}{V_T} slope \left(\frac{\partial V}{\partial log J}\right) \quad (4.11)$$

and saturation current is extracted from intercept. Fig. 4.28 (a) shows the semilog curve of J-V characterization of Ag/PT-BCT/FTO heterostructure. The linear region is fitted to extract the ideality factor η and saturation current J_0. In positive applied voltage region, the saturation current in dark is $5.3x10^{-7}$ A/cm^2 when voltage is more than 2V and under light condition this value is $7.8x10^{-7}$ A/cm^2. In negative applied voltage region, the saturation current is $7.17x10^{-7}$ A/cm^2 and under light it is $6.45x10^{-7}$ A/cm^2. The higher value (>13) is extracted for ideality factor when voltage is more than 2V. This shows Ag/PT-BCT/FTO heterostrucure does not behave as ideal diode for higher applied voltage. When applied voltage is less than -1V, the saturation current is $1.318x10^{-7}$ A/cm^2 is extracted and an ideality factor is 6.72. If we assume that photocurrent is independent of voltage, the open circuit voltage can be also written as $V_{oc} = (2.303\eta kT/q)\log (J_{sc}/J_0)$ [S. R. Cowan et al. (2010)]. Using the extracted parameters η, J_{sc}, and J_0 of log J-V curve in low applied voltage region (0 to -1V), we have extracted V_{oc} = - 0.15 V. As these diodes are not ideal diode and also photocurrent depends on the applied voltage, so, we can say that our experimentally obtained V_{oc} (~ 0.09V) is near to theoretically extracted V_{oc} (-0.15V). To extract the charge mobility, space-charge limited model was applied. A typical log J vs log V characteristic of positive applied voltage branch is illustrated in Fig. 4.28 (b). There are three linear region in logJ - logV curve. The following equation is used to extract mobility 'μ' and charge carrier density 'n' from linear region of curve. The current density is given by Mott-Gurny Law

$$J = \frac{9}{8}\mu\varepsilon_0\varepsilon_r\frac{V^2}{d^3} \quad (4.12)$$

Where μ= mobility (cm^2/vs), d = thickness (in m) of film, J= current density (A/cm^2), ε_r= dielectric permittivity of film [N. F. Mott et al. (1948)]. The current density in terms of mobility can be expressed as J = (nqμV)/d and using this equation charge carrier density 'n' is calculated. The mobility of charge carriers increase from $1.47x10^{-3}$ to 1.88 cm^2/vs under light. The charge carrier density is $1.09x10^{17}$ cm^{-3}. In negative applied region (-5V-0V), the mobility increases from $1.52x10^{-3}$ cm^2/vs to $1.67x10^{-3}$ cm^2/vs under light condition. The log J-log V curve in negative applied voltage region is shown in Fig. 4.28 (c). The ideality factor (η), series resistance (R_s) and barrier height (Φ_B) are extracted using Cheung's model in which slope dV/dlnJ is used [S. K. Cheung et al. (1986)]. The current density formula 4.8 is used. Cheung et al have provided following equations to calculate the R_s, η and after linear fitting.

$$\frac{dV}{dlnJ} = R.A.J. + \frac{\eta}{\beta}, \text{ where } \beta = \frac{q}{kT} \qquad (4.13)$$

$$H(J) = V - \frac{n}{\beta} ln\left(\frac{J}{A^* T^2}\right) \qquad (4.14)$$

$$H(J) = R.A.J + \eta\Phi_B \qquad (4.15)$$

The ideality factor was determined from slope of dV/dlnJ vs J plot as shown in Fig. 4.28 (d) and series resistance is calculated from the intercept. The ideality factor is 1.22 in dark condition and series resistance is 13.04 kΩ. The series resistance is reduced to 3.05 kΩ under light. The increase in current under light can also be attributed to decrease in series resistance. The equation 4.15 is used to calculate the barrier height. The graph between H(J) vs J is plotted as shown in Fig. 4.28 (e). After fitting the linear region, Φ_B is determined from the intercept. Under dark condition Φ_B is 0.6414 eV. Fig.4.28 shows the H(J) vs J plot for photocurrent and it provide Φ_B is 0.538 eV. The lowering Φ_B of is attributed to higher photocurrent under light conditions.

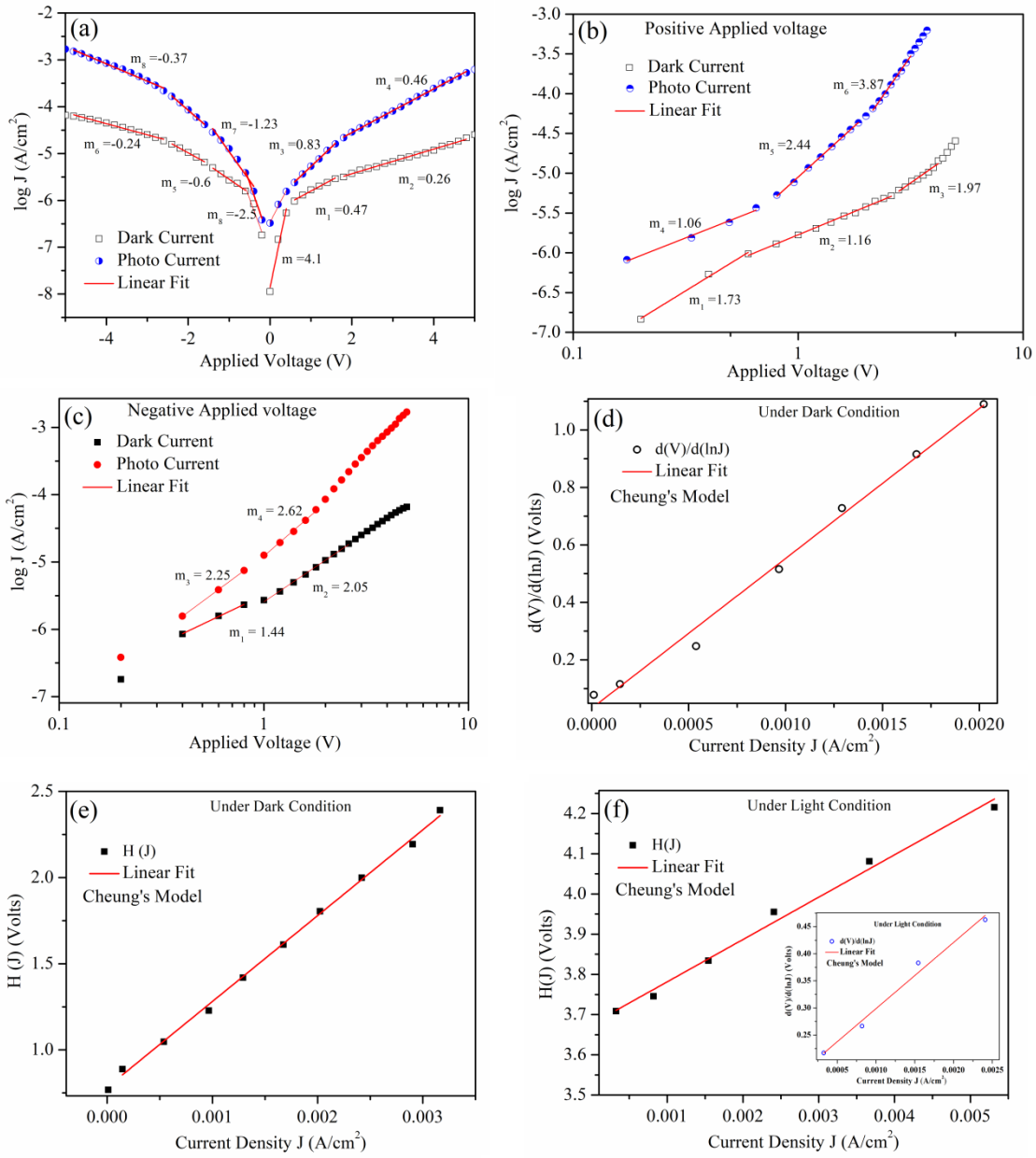

FIGURE 4.28 (a) J-V plots for PT-BCT based diode on a semilog scale. The slopes of linear fit are used to extract ideality factor and saturation current (b) logJ vs logV curve for positive applied voltage region (c) logJ vs logV curve for positive applied voltage region to extract charge mobility μ (d) Plot d(V)/d(lnJ) vs J with linear fit to extract series resistance and ideality factor (e) H(J) vs J plot under dark condition (f) H(J) vs J plot under light condition to extract to barrier potential height Φ_B, inset is showing d(V)/d(lnJ) vs J plot.

4.3.9 Tip-Enhanced I-V Characteristics of PT-BCT/FTO Heterostructure

Here, we report the strain-gradient induced flexo-photovoltaic effect in PT-BCT/FTO heterostructure. Alexe et al have used conductive Pt tip of atomic force microscopy (AFM) as nanoscale top electrode and measured the photocurrent from $BiFeO_3$ single crystal [M. Alexe et al. (2011)]. In order to study the local electrical properties at nanoscale, similar approach is used to collect to non-equilibrium carriers from $0.60PbTiO_3$-$0.40Bi(Co_{0.60}Ti_{0.40})O_3$ (PT-BCT) thin film deposited on FTO substrate. The device structure and measurement circuit are shown in Fig. 4.29 (a). The AFM tip exerts a point force on surface of thin film and simultaneously collected the current from nanoscale contact area [M.–M Yang et al. (2015)]. When AFM tip come in contact with film's surface, a strain gradient generates an electric field in film which is known as the flexoelectric effect. This strain gradient also breaks the inversion symmetry [D. Lee et al. (2011)]. The observations of breaking of inversion symmetry due to strain gradient make it possible to find out bulk photovoltaic effect even in centrosymmetric materials. M.-M Yang et al. have demonstrated the bulk photovoltaic effect in centrosymmetric single crystals of $SrTiO_3$, TiO_2 and Si using the strain gradient and termed it as flexo-photovoltaic effect [M.-M Yang et al. (2018). The Pt tip creates strain induced surface bending at nanoscale on film's surface. Due to flexoelectric effect polarization states are created throughout the film. This polarization develops a depolarization field in film. Strain gradient generated electric field is given by equation $E_s = \frac{q}{4\pi\varepsilon_0 a}\frac{\partial u}{\partial z}$, where q is the electronic charge, ε_0 is the permittivity of free space, $\partial u/\partial z$ is the strain gradient, a is lattice constant of material [A. Gruverman et al. (2003)]. D. Lee et al. have reported flexoelectric effect the polarization in $HoMnO_3$ epitaxial thin films [D. Lee et al. (2011)].

The current-voltage (I-V) characteristics of the PT-BCT/FTO heterostructure under light illumination using green laser light (wavelength = 532 nm) are shown in Fig.4.27 (b). The inset of The Fig 4.29 (b) shows the measurement points on the surface of film. The I-V is measured at various points on surface of the film and it is observed that photocurrent is not much varied. The I-V curve shows deviation from linear behaviour which shows the evidence of Schottky contacts between Pt-tip and ferroelectric layer surface. In order to measure the effect of depolarization field, I-V was also measured for unpoled and poled samples as shown in Fig. 4.29 (c) and (d). In unpoled condition, device shows I_{sc} = 0.3 nA and V_{oc} = -0.19V which got increased to I_{sc} = 1.07 nA and V_{oc} = -0.67V after positive poling. The negatively poled film shows I_{sc} = -1.9 nA and V_{oc} = 0.53V. The enhancement in photocurrent after poling can be related to combined built-in field due to strain and poling. There are two depolarization fields act in PT-BCT film. The PT-BCT film already have inherent polarization which develop a depolarization field $E_{dep} = ((-P-\sigma_s)/\varepsilon)$, P is polarization film, σ_s is screening charge and ε is dielectric permittivity of the film's material [S. M. Park et al. (2020)]. So, two depolarization field (E_s+ E_{dep}) dominates over built-in field due to Schottky interface [M. Wu et al. (2021)]. The observed switchable I_{sc} and V_{oc} parameters confirm the effect of depolarization field on photovoltaic phenomenon in fabricated device using $0.60PbTiO_3$-$0.40Bi(Co_{0.60}Ti_{0.40})O_3$ ferroelectric layer. Fig. 4.30 (a) depicts the schematic diagram of PT-BCT/FTO device structure with C-AFM measurement system showing the strain gradient induced flexoelectric effect using Pt tip. Fig. 4.30 (b) shows the schematic energy band diagram of PT-BCT/FTO heterostructure when Pt tip is in contact with film under conditions (b) without poling (c) with positive poling (d) with negative poling. The field at interface is termed as E_{bi}, depolarization field due to poling E_{pol} and field due spontaneous polarization P generated by strain gradient is termed as

E_{flexo}. Interface induced built-in field at FTO/PT-BCT interface termed as E_{bi2} and at Pt/PT-BCT interface termed as E_{bi1}. In unpoled sample only interface induced built-in field and depolarization filed due to strain gradient play role in separating the charge carriers. As light first reached at Pt/PT-BCT interface, the obtained current is mostly due to flexoelectric induced depolarization field created by Pt tip. In poling conditions, saturation polarization of film also play a role in charge separation and transportation process. The total field become $E_{Total} = E_{flexo}+E_{pol}+E_{bi}$ and in negative poling total field act $E_{Total} = E_{pol} - E_{flexo}+ E_{bi}$. Due to change in effective built-in field in positive and negative poling condition we obtained positive and negative photo-current. In positive poling, V_{oc} is -0.67V and electrons moves towards FTO electrode and thus generate positive current. In negative poling, V_{oc} is +0.53V and flow of electrons is towards Pt tip and negative photocurrent is generated. When The open circuit voltage (V_{oc}) have two components: switchable component ($V_{sw} =[V_{oc+P} -V_{oc-P}]/2$) due to saturation polarization and nonswitchable component ($V_{ns}=[V_{oc+P} +V_{oc-P}]/2$) due flexoelectric induced polarization [Q. Huang et al. (2022)] where V_{oc+P} is open circuit votage obtained during positive poling condition , V_{oc-P} is open circuit voltage obtained during negative during negative poling conditions. In PT-BCT film the switchable component of V_{oc} is + 0.60 V. The nonswitchable component (V_{ns} = ([-0.67+0.14V/2]=-0.14V) exhibits a negative sign. This indicates that depolarization field due to flexoelectric effect act downward. So, in this case, flexo-electric induced depolarization field cause the photovoltaic effect and thus it can be called flexo-photovoltaic effect. Z.-D. LuO et al. have also demonstrated tip enhanced bulk photovoltaic effect in $LaAlO_3/SrTiO_3$ heterostructure [Z.-D. Luo et al. (2019)]. The flexo-photovoltaic effect is also found in 2-D MoS_2 sheets [J. Jiang et al. (2019)], in epitaxial $LaFeO_3$ thin films [Z. Jiang et al (2022)]and in epitaxial $SrBi_2Nb_2O_9$ thin films [H. W. Shin et al. (2019)].

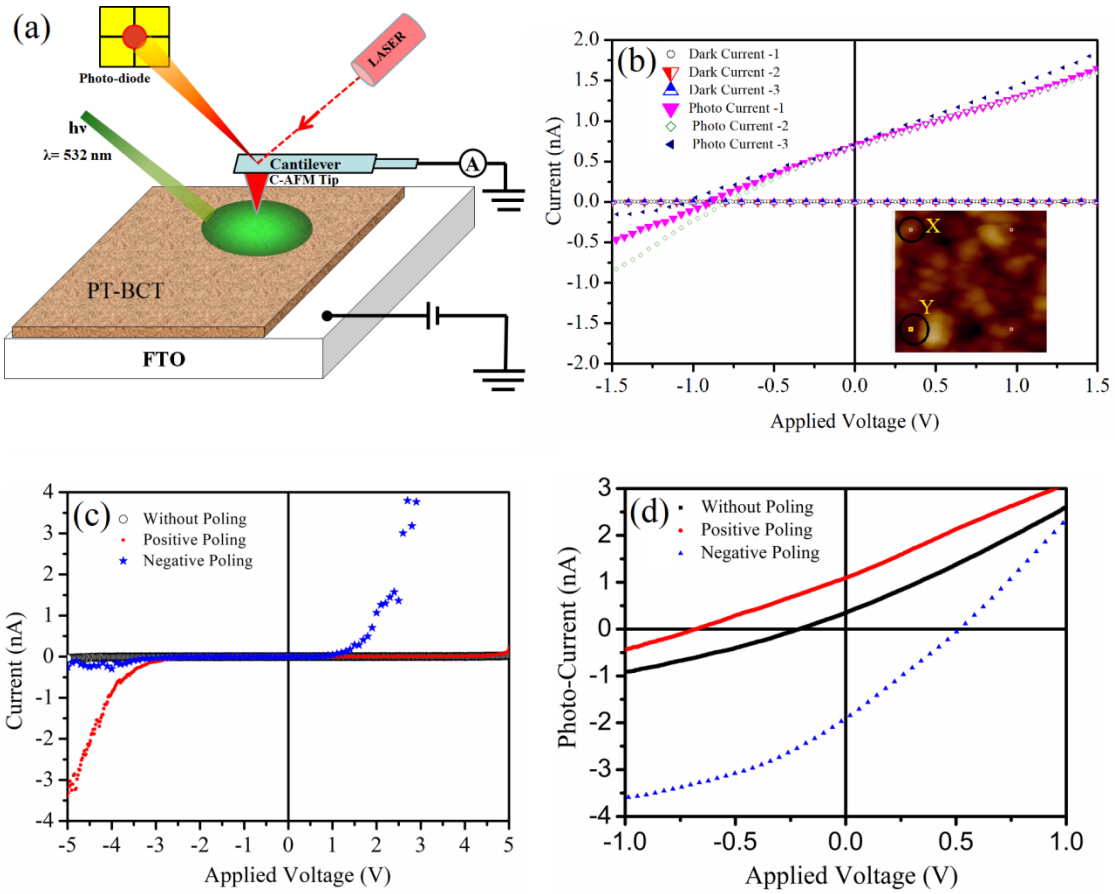

FIGURE 4.29 (a) Schematic diagram of PT-BCT/FTO device structure with C-AFM measurement system (b) Local I-V curve and inset showing the measurement points on the surface (c) Dark I-V curve (d) I-V curve under light of $0.60PbTiO_3$-$0.40Bi(Co_{0.60}Ti_{0.40})O_3$ film surface measured using platinum tip.

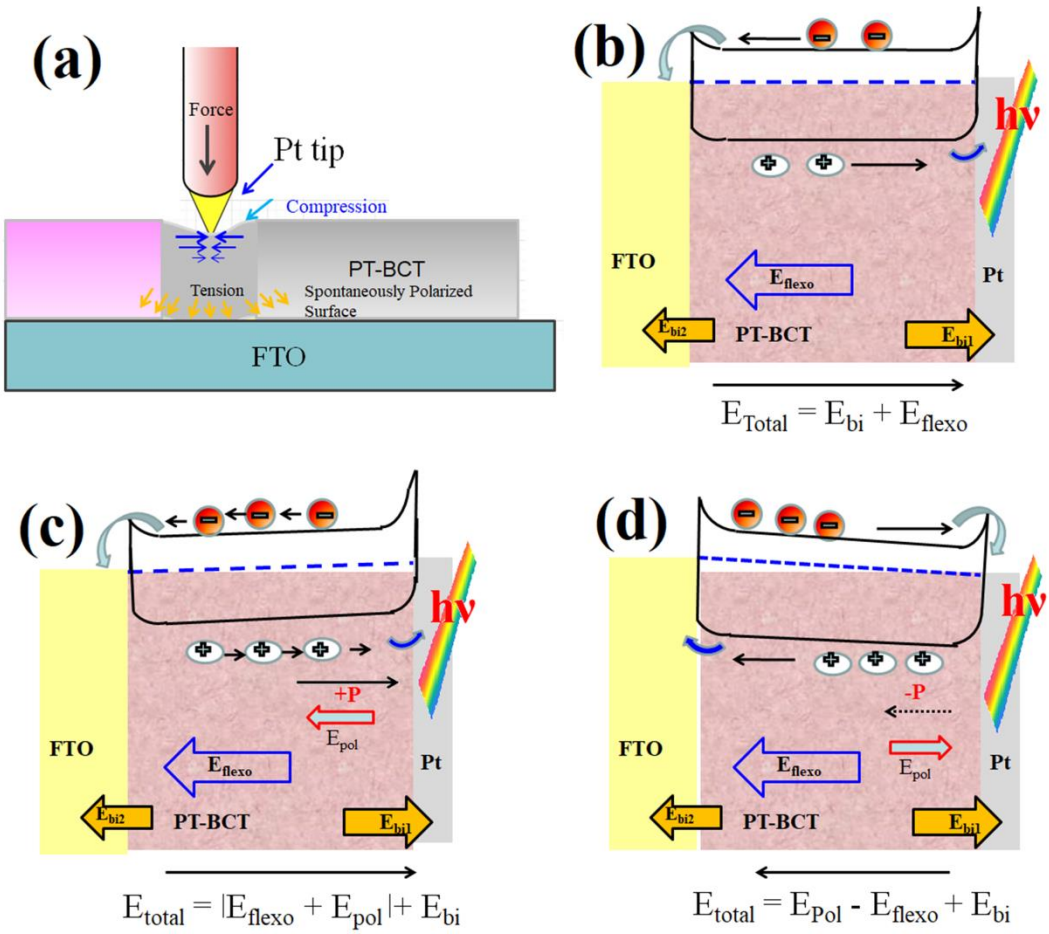

FIGURE 4.30 (a) Schematic diagram of PT-BCT/FTO device structure with C-AFM measurement system showing the strain gradient induced flexoelectric effect using Pt tip. Schematic energy band diagram of PT-BCT/FTO heterostructure when Pt tip is in contact with film under conditions (b) without poling (c) with positive poling (d) with negative poling. The field at interface is termed as E_{bi}, depolarization field due to poling E_{pol} and field due spontaneous polarization P generated by strain gradient is termed as E_{flexo}.

4.4 Conclusions

In this work (Co, Bi) doped $PbTiO_3$ ceramics were successfully prepared by solid state ceramic method and characterized for crystal structure, microstructure and optical properties. The unit cell parameters exhibit significant change with changing calcination temperature. The band gap is significantly reduced for (Bi, Co) doping in $PbTiO_3$. This work provides good insights for the band gap tuning of $PbTiO_3$ with

varying the concentration of Co/Ti. The band gap of material is directly influenced by thermal processing and Co-doping that creates the sub-band region thereby reduces the band gap. The local ferroelectric switching is observed in optimum composition $0.60PbTiO_3$-$0.40Bi(Co_{0.60}Ti_{0.40})O_3$ thin films. The current-voltage (I-V) characteristics of as prepared Ag/PT-BCT/FTO device was measured in dark and under light illumination. The fabricated device shows the Schottky diode-like characteristics and possible conduction mechanism are explained after fitting the J-V data. I-V for $0.60PbTiO_3$-$0.40Bi(Co_{0.60}Ti_{0.40})O_3$/FTO is measured using conducting Pt-tip that reveals switchable flexophotovoltaic effect which explained by analysing the total depolarization field in PT-BCT film due to the strain gradient, saturation polarization and built-in potential due to interface.